

Distribution Agreement

In presenting this thesis or dissertation as a partial fulfillment of the requirements for an advanced degree from Emory University, I hereby grant to Emory University and its agents the non-exclusive license to archive, make accessible, and display my thesis or dissertation in whole or in part in all forms of media, now or hereafter known, including display on the world wide web. I understand that I may select some access restrictions as part of the online submission of this thesis or dissertation. I retain all ownership rights to the copyright of the thesis or dissertation. I also retain the right to use in future works (such as articles or books) all or part of this thesis or dissertation.

Signature:

Cong Cao

Date

Glassy and Jammed Systems: Structures and Dynamics

By

Cong Cao
Doctor of Philosophy

Physics

Eric R. Weeks, Ph.D.
Advisor

Stefan Boettcher, Ph.D.
Committee Member

Justin C. Burton, Ph.D.
Committee Member

Jennifer E. Curtis, Ph.D.
Committee Member

Ajit Srivastava, Ph.D.
Committee Member

Accepted:

Lisa A. Tedesco, Ph.D.
Dean of the James T. Laney School of Graduate Studies

Date: _____

Glassy and Jammed Systems: Structures and Dynamics

By

Cong Cao
B.S., Shanghai Jiao Tong University, Shanghai, 2014

Advisor: Eric R. Weeks, Ph.D.

An abstract of
A dissertation submitted to the Faculty of the
James T. Laney School of Graduate Studies of Emory University
in partial fulfillment of the requirements for the degree of
Doctor of Philosophy
in Physics
2020

Abstract

Glassy and Jammed Systems: Structures and Dynamics

By Cong Cao

Soft materials are usually composed of basic units much larger than atomic scale. For example, colloids are 10 nm to 10 μm solid particles dispersed in a liquid phase; emulsions consist of two immiscible liquids, with one dispersed in another as a droplet form. On one hand, these systems possess similarities with atomic glassy systems; on the other hand, thermal fluctuations and gravity could both play a role in a system's structure and dynamics depending on their components' scale. In this dissertation, we will explore structural and dynamical characteristics of various soft material systems: from $\sim \mu\text{m}$ colloidal suspensions to $\sim\text{mm}$ granular materials; from spherical particles to rods with different aspect ratios. We are curious about the unique properties in each system, while at the same time eager to find connections between different soft materials.

In chapter 2, we use confocal microscopy to study the aging of a bidisperse colloidal glass near rough and smooth boundaries. Near smooth boundaries, the particles form layers, and particle motion is dramatically slower near the boundary as compared to the bulk. Near rough boundaries, the layers nearly vanish, and particle motion is nearly identical to that of the bulk. The gradient in dynamics near the boundaries is demonstrated to be a function of the gradient in structure for both types of boundaries. Our observations show that wall-induced layer structures strongly influence aging.

In chapter 3, we conduct x-ray tomography experiments and study the boundary effect of 3D rod packing (rods packed in a finite cylindrical container). We then compare our tomography results with traditional protocols and simulation results. In all cases, rods pack randomly in cylindrical containers whose smallest dimension is larger than the rod length. Packings in smaller containers have lower volume fractions than those in larger containers, demonstrating the influence of the boundaries. X-ray tomography experiments show that the boundary effects depend on the orientation of the boundary, indicating a strong influence of gravity, whereas the simulation finds boundary effects that are purely geometric. In all cases, the boundary influence extends approximately half a particle length into the interior of the container.

In chapter 4, we study the rheology of monodisperse and bidisperse emulsions with various droplet sizes (1 μm – 2 μm diameter). Above a critical volume fraction ϕ_c , these systems exhibit solid-like behavior and possess a yield stress. Previous experiments suggest that for small thermal particles, rheology will see a glass transition at $\phi_c = \phi_g = 0.58$; for large athermal systems, rheology will see a jamming transition at $\phi_c = \phi_J = 0.64$. However, simulations point out that at the crossover of thermal and athermal regimes, the glass and jamming transitions may both be observed in the same sample. Here we conduct an experiment by shearing four oil-in-water emulsions with a rheometer. We observe both a glass and a jamming transition for our smaller diameter droplets, and only a jamming transition for our larger diameter droplets. The bidisperse sample behaves similarly to the small droplet sample,

with two transitions observed. We fit our data with both Herschel-Bulkley model and Three-Component model. Based on the fitting parameters, our raw rheological data would not collapse into a master curve. Our results suggest that liquid-solid transitions may not be universal, but depends on particle type.

Glassy and Jammed Systems: Structures and Dynamics

By

Cong Cao
B.S., Shanghai Jiao Tong University, Shanghai, 2014

Advisor: Eric R. Weeks, Ph.D.

A dissertation submitted to the Faculty of the
James T. Laney School of Graduate Studies of Emory University
in partial fulfillment of the requirements for the degree of
Doctor of Philosophy
in Physics
2020

Acknowledgments

Throughout finishing all my projects and working on the writing of this dissertation, I have received a great deal of support and assistance.

I would like to thank my mentor and my friend, Prof. Eric R. Weeks. Deep in my heart, Eric is how an outstanding researcher should look like: smart, nice but sharp, eternal youth, along with his own sense of humor. It's my honor to work under Eric's supervision for the past six years. I learned how to be a good student, how to be a good teacher and eventually how to be a good researcher (still in progress) from him. I really enjoy the fun of 'squishy physics' in Weeks' lab and I will bring what I learnt from Eric to my next destination.

I would like to thank my PhD committee, Prof. Justin Burton, Prof. Stefan Boettcher, Prof. Jennifer Curtis and Prof. Ajit Srivastava, for suggestions and feedback you gave me along my PhD career.

I would like to thank my colleagues in Weeks' lab. When I first joined the lab, Dr. Xia Hong, Dr. Xin Du and Dr. Skandar Vivek gave me helpful suggestions and helped me quickly adapt to the lab. Dr. Carlos Orellana, taught me abundant experimental tips about rheometer and emulsions. We were also tennis and table tennis buddies. I would also like to thank Yonglun Jiang, Andy Eddins, Pablo Illing, Julian Freeman, Janna Lowensohn, Mia Morrell, Ran Tao, Jason Jiang, Cory Donofrio, Anisa Hofert, Yijun Dong, Haoran Wang, Steven Rhodes and Jason Boss, for all their support and help along my PhD career. Thanks folks.

I would like to thank my collaborators: Jianshan Liao from Prof. Breedveld's lab, Yixiao Dong from Prof. Salaita's lab, Liqun Ning from Prof. Serpooshan's lab and Xinru Huang from Prof. Roth's lab. These interdisciplinary collaborations broaden my knowledge and help me step out my comfort zone to discover more interesting problems.

I would like to thank my friends in/outside physics department, who share their joy

with me. They fulfill my six-year journey at Emory with fun, laughter and countless memorable moments. Here I want to say that I'm sincerely grateful to have you all in my life!

In addition, I would like to thank my parents, Jianying Huang and Zhangping Cao. I could never pursue and obtain a PhD degree without their support. My parents are both teachers, throughout the past 25 years, they taught thousands of students and helped them go to college. They are the best teachers and role model for me. I'm proud to be their son. I know they are proud of me too.

Lastly, I would like to thank my girlfriend Dongdi Gu, you are the biggest treasure I found throughout my PhD career. I'm lucky to have you by my side.

Thank you all, and may "aging" never happen to you my friends.

Contents

1	Introduction	1
1.1	Soft materials	1
1.2	Packing and soft materials	3
1.3	Jamming and glass transition	6
2	Aging Near Rough and Smooth Boundaries in Colloidal Glass	9
2.1	Introduction	9
2.2	Experimental details	12
2.3	Results	15
2.4	Conclusions	24
3	Random packing of rods in small containers: X-ray tomography experiments	26
3.1	Introduction	26
3.1.1	Random close packing	26
3.1.2	Recent studies on long thin packing	27
3.2	Experimental details	30
3.2.1	Rods and CT scanners	30
3.2.2	Image processing	31
3.3	3D rods results	33
3.3.1	Tomography results	33

3.3.2	Implications of tomography data on bulk parameters	37
3.3.3	Comparison with simulation data	39
3.3.4	Discussion	41
3.4	2D and Sandpaper	41
3.4.1	2D rods packing results	41
3.4.2	Sandpaper results	43
4	Rheology of jammed and glassy materials	47
4.1	Introduction	47
4.2	Experimental details	51
4.2.1	Sample synthesis	51
4.2.2	Measuring volume fraction	54
4.2.3	Measuring particles' size	55
4.2.4	Rheological details	56
4.3	Analysis and results	57
4.4	Conclusion	67
5	Conclusion	69
	Bibliography	72

List of Figures

1.1	Soft materials studied in our lab: (a) dilute colloids samples made by Cong, aimed at determining particles' size. (b) 2D monodisperse emulsions made by Xia Hong, former PhD in Weeks' lab. (c) Creamy 'squishy physics' written by Eric 'The boss' Weeks.(d) hydrogel particles for Mia Morrel's (former lab member, now in NYU) clogging experiments. (e) sandpile picture taken when Cong passed his qualifier. (f) 3D reconstructed acrylic rods in Julian Freeman's (former lab member) experiments.	2
1.2	Schematic figures for face-centered cubic (fcc) and Hexagonal closing packing (hcp) structures in both top view and side view. For the hcp structure, we have a ABAB stacking of such planes. While for the fcc structure, we have a ABCABC layer sequences instead.	4

- 1.3 Two glass/jamming transition diagrams: (a) The three controlled variables are $1/\phi$ (volume fraction), temperature T and shear stress Σ . The states lie in the curves, close to the origin, are jammed state. Along the curve downward in ϕ - T quadrant, the glass transition, happens in high temperature, would extrapolate into jamming transition when thermal motion can be barely ignored. Figure is copied from [107], license number:RNP/20/OCT/031459. (b) The three controlled variables are also $1/\phi$ (volume fraction), temperature T and shear stress Σ . Differently, there is a wing-like structure along T axis, which indicates these two transitions can only be observed separately and will not transit into each other with the change of temperature. When temperature is approach to nearly zero, systems undergo the jamming transition at $\phi = 0.64$. When temperature is high enough, systems undergo the glass transition at a smaller volume fraction $\phi \approx 0.58$. At the crossover regime between thermal and athermal regime, there are possibilities for us to observe glass transition and jamming transition at different volume fraction $\phi_g < \phi_j$. Figure is copied from [66], license number:RNP/20/OCT/031460. 7
- 2.1 Top view and side view for reconstructed 3D images for colloidal samples near (a) a smooth boundary and (b) a rough boundary. Color is a continuous parameter representing particles distances away from the boundary (from 0 to 10 μm). The particles closest to the boundary are on the top and colored dark purple. The grey boxes have dimensions $20 \times 20 \times 15 \mu\text{m}^3$, which is a subset of the full image volume. While the sample has particles of two sizes, only the large particles are visible in the experiment. The data are pictured at $t_{\text{age}} = 10 \text{ min}$ 15

- 2.2 The local number density $n(z)$ as a function of the distance from the boundary at $z = 0 \mu\text{m}$ for samples near (a) a smooth boundary and (b) a rough boundary. Layer-like structures are observed in both samples in first few layers, although they are sharper for the smooth boundary and persist to larger z . The vertical dotted lines indicate separate layers, with a fixed spacing once the layers become ill-defined. The red horizontal lines show the average number density in the region $z > 10 \mu\text{m}$ 16
- 2.3 The mean square displacement for motion parallel to the boundaries calculated as $\Delta r_{xy}^2 = \frac{1}{2} \langle \Delta x^2 + \Delta y^2 \rangle$. The data are averaged over four different t_{age} regimes as indicated. Data are for (a) 1st layer with a rough boundary, (b) 4th layer with a rough boundary, (c) 1st layer with a smooth boundary, (d) 4th layer with a smooth boundary. The data for the 4th layers match the bulk behavior, and their progression to larger time scales with increasing t_{age} demonstrates that the sample is aging. The data for the 1st layers show that aging is fairly unchanged for the rough boundary (a), but markedly different for the smooth boundary (c). 18
- 2.4 The mean square displacement along the direction perpendicular to the boundary (z) calculated during four different t_{age} regimes as indicated. Data are for (a) 1st layer with a rough boundary, (b) 4th layer with a rough boundary, (c) 1st layer with a smooth boundary, (d) 4th layer with a smooth boundary. 19

2.5	Average distance particles move over $\Delta t = 20$ min, as a function of aging time t_{age} . The curve colors indicate the layer number as labeled in panels (e,f). Panels show data for motions parallel to the boundary ($1/2\langle x^2 + y^2 \rangle$) and perpendicular to the boundary ($\langle z^2 \rangle$) for rough and smooth boundaries as indicated. In panels (e,f) the data are normalized by their initial values.	20
2.6	(a) The t_{age} average of Δz^2 for the last 15 min of Fig. 2.5(b,d) plotted as a function of z , with the average done over all particles in a layer (as defined in Fig. 2.2). The z value is the center of each layer over which the average is taken. (b) The same data normalized by the mean value of Δz^2 for $t_{\text{age}} \leq 5$ min. This represents the slowing seen due to aging; the data close to 1.0 show little or no aging behavior. The error bars represent the variability in the results when different ranges for the t_{age} -averaging are used.	22
2.7	The large t_{age} motion in z plotted as a function of the standard deviation of number density σ_n over the mean number density $\langle n \rangle$ where these quantities are defined within each layer (see Fig 2.2). The data for the vertical coordinate correspond to that of Fig. 2.6(b).	23
3.1	X-ray tomography data of rods with length $L = 2.57$ cm, aspect ratio 8 in a container with $R = 13.2$ cm $\approx 5.2L$ and $H = 7.4$ cm $\approx 2.9L$. (a) X-ray image showing horizontal cross section through the container. (b) Vertical cross section, where the white voxels are those above a threshold intensity. The smallest white dots are the corners of rods. (c) 3D rendering of the tomography data.	31
3.2	We take four steps to obtain the reconstructed packing: We remove container's boundary and segment the rods from (a) to (b); we then reconstruct the packing and set a 'fake' top boundary from (c) to (d).	32

3.3 (a) Volume fraction $\phi(z)$ as a function of distance z from the bottom boundary and (b) volume fraction $\phi(r)$ as a function of distance r away from the central axis. These data correspond to a short wide container with diameter $2R \approx 4.9L$ and height $H \approx 2.9L$. In figure (a), the red and blue shaded regions represent the top and bottom boundary layers, with boundary thickness of $\delta L = 0.5L$ (estimated by eye). In figure (b), the blue shaded area represents the side boundary layer, with a smaller boundary thickness $\delta L = 0.3L$ (again estimated by eye). Both z and r are normalized by rod's length L 33

3.4 (a) $\phi(z)$ as a function of distance z away from the bottom boundary and (b) $\phi(r)$ as a function of distance r away from the central axis. These data correspond to a short narrow container with diameter $2R \approx 1.9L$ and height $H \approx 2.9L$. All three boundary layers have the same thickness as the data shown in Fig. 3.3, as well as the same bulk value of ϕ_∞ 34

3.5 Nematic order parameter S as a function of vertical position z/L for the large ($2R = 4.9L$) and small ($2R = 2.9L$) containers as indicated. $S = -1/2$ corresponds to horizontally aligned rods, and $S = 0$ corresponds to isotropically oriented rods. 35

3.6 The nematic order parameter S as a function of the distance r/L away from the center axis. The blue shaded region represents the side boundary layer; compare with Figs. 3.3(b) and 3.4(b). The inset graph is an expanded view of the large container data. 36

3.7	Local packing fraction ϕ/ϕ_∞ as a function of distance from the nearest boundary, averaged over all aspect ratios from the simulation data. The circles are as a function of $R-r$, and the squares are as a function of z . Inset: Data from specific aspect ratios $\alpha = 4$ (light violet diamonds), 16 (green upward triangles), and 32 (dark violet downward triangles).	40
3.8	Nematic order parameter as a function of distance from the top or bottom boundary, from the simulation data averaged over aspect ratios 4 and 12.	40
3.9	2D experimental set-up, designed by JO Freeman	42
3.10	Nematic order parameter S as a function of vertical position y/L for 2d packing. $S = -1/2$ corresponds to horizontally aligned rods, and $S = 0$ corresponds to isotropically oriented rods.	43
3.11	The nematic order parameter S as a function of the distance x/L away from the boundary.	44
3.12	We pour rods into containers with sandpaper (from left to right): First, we attach sandpaper to container's inner wall; Second, we pour rods gently into containers; Last, we remove rods on top gently.	45
3.13	Volume fraction $\phi(z)$ as a function of distance z from the bottom boundary for both smooth (15k) and rough boundary condition (60grit).	45
3.14	Volume fraction $\phi(r)$ as a function of distance r away from the central axis with smooth boundary condition (15k) and rough boundary condition (60grit).	46
4.1	Monodisperse emulsions (silicone oil + water) obtained by fractionation methods, the mean diameter is around $2 \mu m$. Image was taken by Leica DM IRB research microscope.	52

4.2	(a),Polystyrene particles ($d= 2 \mu m$ observed under Leica DM IRB research microscope. (b) swelled emulsions observed under same conditions (average diameter is around $6 \mu m$).	53
4.3	TPM emulsions polymerized by AIBN and observed under SEM (a) Monodisperse sample with $d_{\text{mean}}=1.16 \mu m$ (b) Bidisperse sample with diameter $d_{\text{small}}=1.06 \mu m$, $d_{\text{large}}=1.86 \mu m$. Sub-nano particles were only observed after polymerization and may be due to unreacted TPM oil.	54
4.4	Shear stress σ_y plotted as a function of strain rate $\dot{\gamma}$ for (a) $2.04\mu m$ monodisperse sample, (b) $1.16\mu m$ monodisperse sample, (c) $1.06/1.86\mu m$ bidisperse sample. The rheological curves are labeled by their volume fractions ϕ . The solid lines are fitting curves with Herschel-Bulkley model, and the dotted lines are fitting with TC model [20]. The red dashed lines are guidelines that identify the transition between samples with and without a yield stress.	58
4.5	The HB and TC model fitting parameters as a function of volume fraction ϕ for $1.16/2.03 \mu m$ samples: n as a function of ϕ for (a) $1.16 \mu m$ sample, (b) $2.03 \mu m$ sample; η_{bg} as a function of ϕ for (c) $1.16 \mu m$ sample, (d) $2.03 \mu m$ sample. Green shadow region represents that when fit $\eta_{bg}=0$, it would only have less than 1 % difference in fitting error than best fitting parameter; $\dot{\gamma}_c$ as a function of ϕ for (e) $1.16 \mu m$ sample, (f) $2.03 \mu m$ sample. Yellow shadow region represents that when fit $\dot{\gamma}_c = \infty$, , it would only have less than 1 % difference in fitting error than best fitting parameter; σ_y as a function of ϕ (g) $1.16 \mu m$ sample, (h) $2.03 \mu m$ sample. Filled circles are σ_y from TC model, and + signs are σ_y from HB model, most of the time there are no obvious difference between two fittings.	60

- 4.6 (a) The yield stress σ_y as a function of volume fraction ϕ for our experimental data; each set of data is labeled by the mean droplet diameter. The red asterisk data are for the bidisperse sample, labeled by the two mean droplet diameters. The effective temperature ranges from $T_{\text{eff}} = 5 \times 10^{-6}$ for the $d = 1.03 \mu\text{m}$ sample to 1.3×10^{-6} for the $d = 2.03 \mu\text{m}$ sample; see text for details. The dashed lines are exponential fit curves $\sigma_y = \sigma_0 e^{C\phi}$ with $\sigma_0 = 3 \times 10^{-17}$ Pa, $C = 60$ for small particles and $\sigma_0 = 2 \times 10^{-21}$ Pa, $C = 70$ for the larger particles.[74], σ_0 is a fitting parameter with no deep physical meaning behind. (b) Simulation results from Ref. [66]. As ϕ is decreased, the system goes through the jamming transition at around 0.64, with an abrupt drop in yield stress. After that, it will stay in a glassy regime, with only a moderate decrease of the yield stress until it reaches the glass transition point $\phi_g \approx 0.58$, at which point the yield stress vanishes [66]. The red dashed line represents the $T = 0$ limit (for large, athermal particles). For the black curves, the effective temperature varies by factors of ten, ranging from the top black curve (“Fluid,” $T_{\text{eff}} = 10^{-4}$ to the bottom black curve (“Glass,” $T_{\text{eff}} = 10^{-7}$). 61
- 4.7 (a) The yield stress as a function of ϕ , with yield stress nondimensionalized by the thermal energy $k_B T$. (b) The yield stress as a function of ϕ , with yield stress nondimensionalized by the oil-water surface tension Σ . The legend indicates the droplet diameter d and the source of the data, if not our work.[91, 34] 64

Chapter 1

Introduction

1.1 Soft materials

Soft materials are everywhere. Imagine that you just finish a day's work and arrive at your apartment, you open a package full of foam, drink a cup of milk, along with a slice of cheesecake. After that you brush your teeth with toothpaste and shave your beard with creams. Yes, you are surrounded by soft materials! Soft materials, also called soft matter, are defined as materials that possess both solid-like and liquid-like behaviors. They consist of units that are much larger than atom-level but smaller than its macroscopic size [99]. On one hand, these systems share a large amount of similarities with atomic systems (glassy materials), for example, they are dissipative, far from equilibrium and somewhat affected by thermal energy; on the other hand, with a much larger scale, novel phenomena can be observed in real space, since dynamics are slow enough to be tracked in experiments and larger units make particles observable under microscope [22, 159]. Soft materials also possess unique properties themselves due to larger component particles: gravity plays a more important role in some systems [67]; unique patterns are formed at the meso-scale [131]; materials can even retain a memory or behave actively to self-assemble [86].

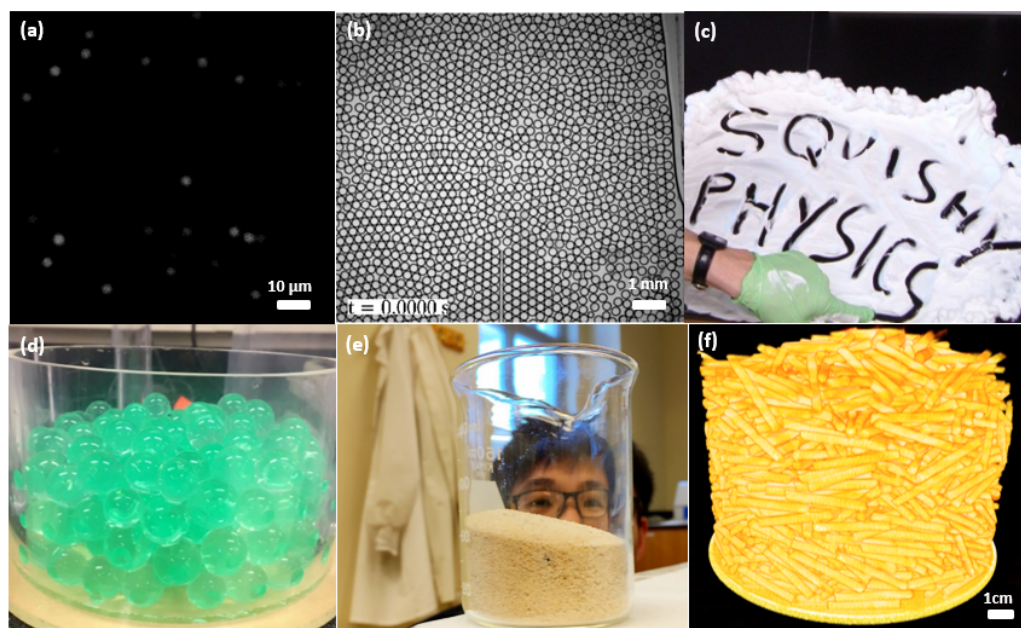


Figure 1.1: Soft materials studied in our lab: (a) dilute colloids samples made by Cong, aimed at determining particles' size. (b) 2D monodisperse emulsions made by Xia Hong, former PhD in Weeks' lab. (c) Creamy 'squishy physics' written by Eric 'The boss' Weeks. (d) hydrogel particles for Mia Morrel's (former lab member, now in NYU) clogging experiments. (e) sandpile picture taken when Cong passed his qualifier. (f) 3D reconstructed acrylic rods in Julian Freeman's (former lab member) experiments.

A variety of soft materials has been studied in our lab, including colloidal suspensions, emulsions, creams, hydrogels and sands (figure 1.1). A colloidal suspension is a heterogeneous system made from solid particles in a liquid, typically $10\ \mu\text{m}$ size or smaller (small enough to undergo Brownian motion). Another soft amorphous solid can be found in emulsions: these are composed of liquid droplets dispersed in another immiscible liquid, with droplet sizes ranging from $10\ \text{nm}$ up to a few hundred μm [92]. Surfactant molecules are needed for stabilization and sample can last for months. A granular material such as sand or hydrogel, is comprised of solid particles, typically mm or larger sized. Brownian motion can be neglected in granular systems, while friction and gravity play a more important role.

In this dissertation, we study colloidal suspensions, acrylic rods and emulsions and discover their unique properties at different scales. In chapter 2, we study binary colloidal suspensions and focus on out-of-equilibrium dynamics (aging behavior). In chapter 3, we investigate structure characteristics of 3D acrylic rods. With the help of CT tomography, we can accurately find centroid and orientation of each rod and determine its structure near the boundary with existence of gravity. In chapter 4, we shear different sizes of emulsions to determine how thermal fluctuations would affect emulsions' rheological properties.

1.2 Packing and soft materials

People started to be curious about the packing problem since 16th century, when sir Kepler promoted the famous conjecture: how many cannon balls can be put into a finite container? Volume fraction ϕ , defines as the ratio between the volume of balls and the volume of the container, perfectly represents how dense balls pack. It turns out that face-centered cubic (fcc) and hexagonal closing packing (hcp) have the highest volume fraction (around 0.740), see Fig. 1.2. It was not until 1998, 300

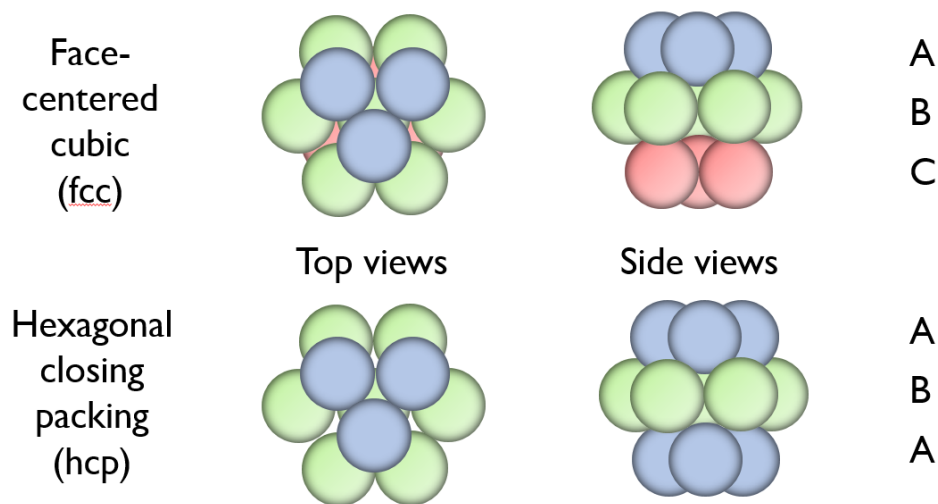


Figure 1.2: Schematic figures for face-centered cubic (fcc) and Hexagonal closing packing (hcp) structures in both top view and side view. For the hcp structure, we have a ABAB stacking of such planes. While for the fcc structure, we have a ABCABC layer sequences instead.

years later, the problem was mathematically proven by Thomas Hales, using complex computer calculations. However, when balls are poured into a container, instead of arranging themselves into hcp or fcc structures, usually they place themselves disorderly with no obvious repetitive units ($\phi_{rcp} = 0.636$). These structures, defined as random close packing (rcp), have great scientific importance. They have been widely studied by researchers across different fields to better understand the structures of living cells, granular materials, emulsions, and colloidal suspensions, to name a few.

In 1964, Bernal [13] employed the hard sphere model to study the structures of liquids. Since then, soft materials packing, including colloids, emulsions and granular media have been studied as a model for phases of matters. Experiments conducted in 1960s and 1970s further proved that hard sphere packings can be analogous to real atomic systems [75, 58]. For the following decades a series of works have been conducted to investigate liquid and crystal structures using colloidal systems [1, 87, 119]. In 1982, Lindsay and Chaikin employed binary samples (mixed two different sizes colloids) to stimulate glassy structures and behaviors [80], which agreed with simulation

results [126]. 5 years after, Pusey and van Megan observed hard-sphere liquid-solid transition in dense uncharged colloids suspensions [119]. Nowadays colloidal packing is widely studied as a model of liquid-solid transition. Volume fraction ϕ and the interaction between particles are the key control parameter [158]. With pure repulsive interaction, when ϕ is lower than 0.494, system would behave like a liquid. When the system is forced to increase ϕ fast enough and is somewhat polydisperse, it would be quenched into supercooled or glassy state, with an amorphous structure. The upper boundary for the glassy regime is $\phi < \phi_{rcp} = 0.636$. The other solid phase is colloidal suspensions with ordered structure, like fcc or hcp. We define it as colloidal crystal, since it shares abundant structure similarities with crystalline solids (like metal). More details about transition between different phases will be discussed in next section.

Boundary conditions play an essential role in soft material packing, from sub-nano particles to millimeter sand grains. In small scale systems, the presence of boundaries have a large influence upon the local dynamics near the boundary [57]. In large scale systems, a recent investigation by Desmond and Weeks used simulations to study the packing of bidisperse random close packed samples [30]. They observed that the sample tended to have a lower local volume fraction against the smooth boundaries than the bulk area. In chapter 2, we investigate impacts brought by both smooth and rough boundary conditions in a binary colloidal suspension and focus on how dynamics of colloids change when changing boundary conditions. We demonstrate that rough walls would greatly diminish the layer-like structures compare to smooth walls. We further discover the correlation between layer-like structures and particle motions perpendicular to the wall. In chapter 3, we study 3D rods packing with CT tomography and determine how bottom boundary and side boundary affect rod's structure separately. We test Desmond-Weeks model and confirm a generalization of the Desmond-Weeks model works for the non-spherical particles (rods).

1.3 Jamming and glass transition

As described in previous sections, soft materials can possess both liquid-like and solid-like properties under certain circumstances. When changing appropriate conditions, systems can undergo a transition from liquid-like (can easily flow) to solid-like (deform elastically and can maintain certain shape). One key characteristic of this transition is the occurrence of yield stress: yield stress defines as the finite stress applied to the system above which the system can start to deform. In 1998, Andrea Liu and Sidney Nagel suggested a universal framework to describe all transitions from the unjammed state to the jammed state. They suggested three key controlled variables that dominate the transition process: temperature, shear stress and volume fraction. Unjammed systems can be tuned into jammed systems by decreasing temperature, decreasing applied stress or increasing the volume fraction. They also defined the jamming transition and glass transition: when yield stress start to occur in athermal systems (such as in granular materials where Brownian motion doesn't matter), systems go through a jamming transition; similarly, when yield stress starts to occur in thermal systems (colloidal suspensions or sub-micro emulsions), we define the process as glass transition. They predicted that glass transition would extrapolate into jamming transition when decreasing temperature and two transitions happen at around same volume fraction, see Fig. 1.3(a). They also suggested there may lie a series of universal physics principles in all these transitions.

However it has been noticed for a long time that granular media tends to have a high critical transition volume fraction ($\phi_c \approx 0.64$) than smaller scale systems, such as colloidal suspensions or emulsions ($\phi_c \approx 0.58$). The discrepancy in ϕ_c was directly addressed in simulations [66], which showed that instead of extrapolating into each other, there is a wing-like structure between the glass transition and jamming transition in crossover regime, see figure 1.3(b). Ref. [66] predicted that such phenomena can be observed by shear dense emulsion samples from 1 - 10 μm [66]. Particle soft-

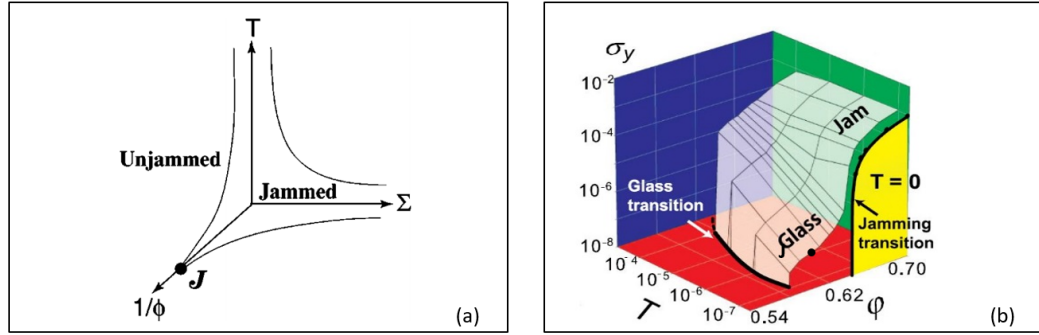


Figure 1.3: Two glass/jamming transition diagrams: (a) The three controlled variables are $1/\phi$ (volume fraction), temperature T and shear stress Σ . The states lie in the curves, close to the origin, are jammed state. Along the curve downward in ϕ - T quadrant, the glass transition, happens in high temperature, would extrapolate into jamming transition when thermal motion can be barely ignored. Figure is copied from [107], license number:RNP/20/OCT/031459. (b) The three controlled variables are also $1/\phi$ (volume fraction), temperature T and shear stress Σ . Differently, there is a wing-like structure along T axis, which indicates these two transitions can only be observed separately and will not transit into each other with the change of temperature. When temperature is approach to nearly zero, systems undergo the jamming transition at $\phi = 0.64$. When temperature is high enough, systems undergo the glass transition at a smaller volume fraction $\phi \approx 0.58$. At the crossover regime between thermal and athermal regime, there are possibilities for us to observe glass transition and jamming transition at different volume fraction $\phi_g < \phi_j$. Figure is copied from [66], license number:RNP/20/OCT/031460.

ness would be a key parameter here since it implies how easily the sample would be deformed by shear motion/thermal motion.

To discover how thermal motion affects these two critical transitions, in chapter 4, we measure rheological behavior for both monodisperse and bidisperse dense emulsions with droplet diameters ranging from 1-2 μm . By tuning particles' size, we aim at exploring the crossover regime between thermal and athermal systems. We also explore how polydispersity affects the transition process. Interestingly, our data support Fig. 1.3 (b): we observe glass transition and jamming transition at different volume fraction; we also observe that critical transitions happen at a different volume fraction, heavily dependent on particles' size.

Chapter 2

Aging Near Rough and Smooth Boundaries in Colloidal Glass

Adapted from Cong Cao, Xinru Huang, Connie B. Roth, and Eric R. Weeks, Aging near rough and smooth boundaries in colloidal glasses, *J. Chem. Phys.*, **147**, 224505 (2017).

2.1 Introduction

Glasses are solids with disordered structures and slow internal dynamics. Efforts to understand the influence of boundaries on glassy dynamics has been an active area of research for more than two decades [4, 44, 124, 128, 9, 36, 101, 64]. Initial efforts on confined systems were thought to provide a route to accessing postulated growing length scales associated with cooperative motion [9, 15, 73, 135, 120, 55, 78, 132, 133]. However, the study of such small system sizes necessitates the presence of boundaries and it has turned out that the specific details of such interfaces have a great deal of influence on the local dynamics near the boundary [57]. In experimental material systems, the type of interface often plays a dominant role over finite size effects where interfacial energy, specific chemical interactions, and substrate compliance are all

factors that have shown to have some influence on the dynamics [47, 147, 110, 118, 127, 39, 6, 156, 23, 37, 65, 7]. In computer molecular dynamics (MD) simulations where the specific details of the boundary need to be constructed at its most basic level, it is unclear a priori how best to accomplish this.

Early MD efforts started with smooth, structureless walls where the boundary was treated as a continuum and details of the wall potential were integrated over in the lateral (x,y) direction leaving only a z -dependence perpendicular to the boundary.[9] Alternatively, molecularly structured walls assembled from Lenard-Jones (LJ) particles into either crystalline arrays or frozen amorphous structures were also investigated [73, 135, 136, 56, 28, 151]. In these simulations, local dynamic near the boundary were usually different than bulk, but the underlying cause why was frequently unclear. Smooth walls typically exhibit faster dynamics than bulk in part because there is no penalty for the particles to slide laterally along the wall [15, 153, 152, 114, 54], a type of motion only considered to be experimentally relevant for a free surface.[114] Systems with molecularly structured walls, where lateral sliding is inhibited, typically exhibited slower dynamics in comparison [73, 135, 55, 136, 56, 140].

One of the major challenges with such boundaries is that for mixtures of LJ particles or polymeric bead-spring models (the most commonly modeled systems), the presence of the wall creates layering of the particle density $\rho(z)$ as a function of distance from the wall[9]. Intuitively, the particles pack easily in a layer against the wall, and then the particles in the second layer pack against that first layer, *etc.*, with the influence of the wall diminishing farther away. Thus, a major effort in these studies is the need to determine the extent to which the observed differences in local dynamics a distance z to the boundary are influenced by the local $\rho(z)$ structure in density. In some cases slower dynamics near the boundary has been associated with a significantly increased local density [9, 42], while other studies have demonstrated that the change in dynamics near the boundary is unrelated to the

$\rho(z)$ density profile [73, 135, 56, 54]. For example, even efforts to construct a neutral boundary that avoids local perturbations to the particle density by freezing in an amorphous, liquid-like structure still leads to perturbations in the local dynamics [73, 135, 136, 16, 79, 60, 59]. It is important to note that local perturbations to the $\rho(z)$ structure are not limited to only coarse-grained simulations, they are also observed in nearly-atomistic, united-atom models [63]. In addition, experimental studies on glassy thin film systems are also trying to uncover the extent to which molecular ordering occurs near a boundary and its possible influence on the local density and dynamics [51, 139, 100, 50, 61].

Here we present a direct experimental comparison of local glassy dynamics next to rough and smooth boundaries using colloidal glasses, which have been previously suggested as a means of experimentally verifying these observations from coarse-grained MD simulations of boundaries [64, 42, 104]. Colloids are small solid particles in a liquid, where Brownian motion allows particles to diffuse and rearrange [64]. We use confocal microscopy to study the aging of a bidisperse colloidal glass where layer-resolved dynamics as a function of distance from a rough or smooth wall are compared with the measured $\rho(z)$ density profile. Smooth boundaries are simply a normal untreated glass coverslip, while rough boundaries are constructed by melting a small amount of the colloidal sample to the coverslip. These stuck particles cover approximately 30-50% of the surface and provide a roughness scale comparable to the particle size. The particle-glass and particle-particle interactions are purely repulsive and so the main difference in the boundary conditions is the topography. We observe distinctly different results between smooth and rough boundary conditions: near smooth boundaries motion is dramatically slower, whereas near rough boundaries the aging process is nearly independent of the distance from the boundary. We ascribe this to the strong influence of layer-like structures formed near the smooth boundary.

Our samples are aging: unlike many phases of matter, glasses are out of equilib-

rium, and so their properties slowly evolve, perhaps toward a steady state [142, 150, 117, 122]. These properties can include the density, enthalpy, and diffusive motion of the molecules comprising the glass. This has implications for the usage of glassy materials which have properties that depend on age perhaps in an undesirable way [144, 62, 117]. Aging has been observed in polymer glasses [117, 144], granular systems [72, 123], and soft materials such as colloids and foams [150, 38, 88, 24, 26, 85, 8, 94, 32]. While for polymer glasses and granular materials aging is often measured as slight decreases in volume, colloidal glasses are typically studied at constant volume. The main signature of aging of colloidal glasses is the dramatic slowing of particle motion as the sample ages [150, 38, 88], often characterized by the slowing down of the mean square particle displacement for time windows at increasing aging times [26]. Previous work suggests that aging in colloidal systems may relate to the local structure around rearranging particles [85] or domains of more mobile particles [26, 163]. In general, it is not surprising that confined glasses age in different ways from their bulk counterparts [117]. In this manuscript we show that aging of colloidal particles is tied to layering structure imposed by the nearby sample boundaries.

2.2 Experimental details

In our experiment we use sterically stabilized poly(methyl methacrylate) (PMMA) particles [5, 119] to prevent aggregation. Two different sizes of particles are mixed in order to prevent crystallization, with $d_L = 2.52 \mu\text{m}$ and $d_S = 1.60 \mu\text{m}$. The particles have a polydispersity of 7%. The number ratio is approximately 1 : 1. To match the particles' density and refraction, we use a mixture of decalin and cyclohexylbromide as the solvent [35]. We view our samples with a fast confocal microscope (VT-Eye from Visitech, International). The large particles are dyed with rhodamine dye and thus are visible, while the small particles are undyed and thus unseen. Based on prior

work, we expect that both small and large particles have similar behavior [85, 103]. Visual inspection using differential interference contrast microscopy, which can see both particle types, confirms that the particles are well-mixed even at the boundary. The imaged volume is $50 \times 50 \times 20 \mu\text{m}^3$. These images are taken once per minute for 2 hours. Our scanning volume starts about $5 \mu\text{m}$ outside the boundary to ensure we have clear images of the particles at the boundary. The microscope pixel size is $0.11 \mu\text{m}$ in x and y (parallel to the boundary) and $0.2 \mu\text{m}$ in z (perpendicular to the boundary). We use standard software to track the motion of the particles in 3D [27, 35]. Our particle locations are accurate to $0.10 \mu\text{m}$ initially and to $0.15 \mu\text{m}$ by the end of the experiment after some photobleaching occurs, which is good enough for particle tracking.

We construct two types of sample chambers. The first uses a normal untreated coverslip as a smooth boundary. The second is prepared by taking a small amount of colloidal sample and melting this on to the coverslip, using an oven at 180°C for 20 min. After this process, the PMMA particles are irreversibly attached to the coverslip. We also tried hydrofluoric acid (HF) to erode coverslip's surface, but it doesn't work as well as we expected. We observed scratches in coverslips surface via transmission electron microscope (TEM). However, the root mean square (RMS) of surface roughness is too small comparing to the size of the colloids (10 times less). Besides, the erosion process is hard to control, thus it's hard for us to get reproducible results. As a result, we abandoned the HF method.

This sample is the same bidisperse mixture of PMMA particles as the main sample with the exception that both particle sizes are undyed. By image analysis we determine that the stuck particles cover approximately 30-50% of the surface (see 2.1). The specific fraction is difficult to measure as we only image the large fluorescently dyed particles, so we cannot see either the smaller mobile particles of our bidisperse sample or the stuck particles of either size. After adding the samples, we never ob-

serve any of our sample particles stuck to the boundaries for either smooth or rough boundary conditions.

We add a stir bar inside each sample chamber so that we can shear rejuvenate the samples [26] and thus initiate the aging process and set $t_{\text{age}} = 0$ (when we stop stirring). Note that t_{age} is set by the laboratory clock and thus is identical throughout our sample; we are not considering the idea of a spatially varying time scale. We find the stirring method gives reproducible results similar to prior work [26, 85], although this is probably different from a temperature or density quench as is usually done for polymer and small molecule glasses [93]. Given the flows caused by the stirring take 20-30 s to appreciably decay after stirring is stopped, there is some uncertainty in our $t_{\text{age}} = 0$, but we examine the data on time scales at least ten times larger than any uncertainty of this initial time.

Confocal microscopy allows us to measure the bulk number density for large particles, which we find to be 0.32 ± 0.03 . The uncertainty represents the variability that we see from location to location. Given that we cannot directly observe the small particles, the observed number density in any given location is not a useful measure of the local volume fraction. Thus, we do not have a direct measure of the volume fraction. Given that the samples behave as glasses (to be shown below) and particles are still able to move, we conclude $\phi_{\text{glass}} < \phi < \phi_{\text{rcp}}$, with $\phi_{\text{glass}} \approx 0.58$ for bidisperse colloidal glasses[103]) and $\phi_{\text{rcp}} \approx 0.65$ (the value for random close packing for our bidisperse sample[31]). Our goal is to have identical samples here by filling both samples from the same stock jar. On the other hand, it's difficult to pipette samples when $\phi > \phi_g$. Therefore, it is important to note that we cannot definitely establish if our two samples are at the same ϕ or, if not, which one would be higher. Luckily, prior studies of aging colloidal glasses found little [89] or no [26] dependence of the behavior on ϕ .

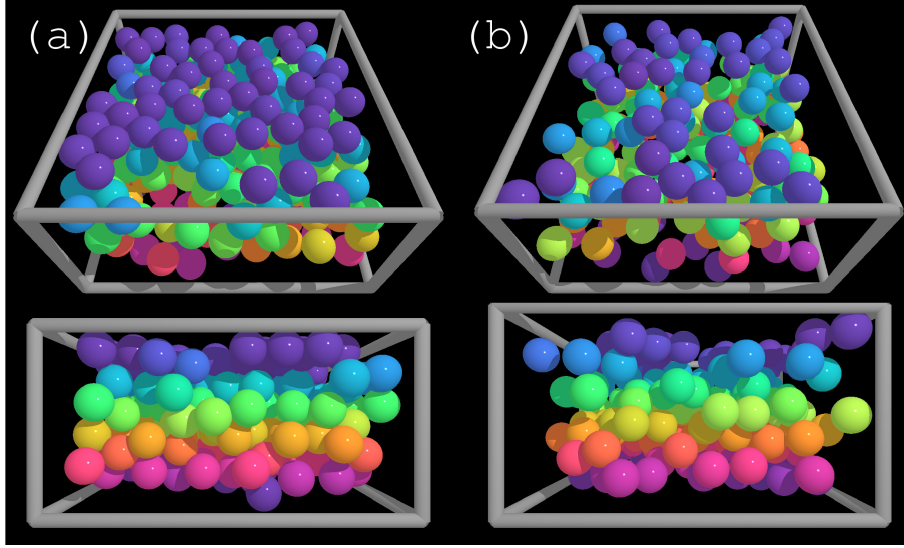


Figure 2.1: Top view and side view for reconstructed 3D images for colloidal samples near (a) a smooth boundary and (b) a rough boundary. Color is a continuous parameter representing particles distances away from the boundary (from 0 to 10 μm). The particles closest to the boundary are on the top and colored dark purple. The grey boxes have dimensions $20 \times 20 \times 15 \mu\text{m}^3$, which is a subset of the full image volume. While the sample has particles of two sizes, only the large particles are visible in the experiment. The data are pictured at $t_{\text{age}} = 10 \text{ min}$.

2.3 Results

Figure 2.1 shows reconstructed 3D images for smooth (a) and rough (b) boundaries. To show the influence of the boundaries, the particles closest to the boundary are on the top of these pictures (colored dark purple). The color changes continuously as a function of the distance z away from the boundary. However, the particles shown in Fig. 2.1(a) appear to have discrete colors as they form layers with distinct z values. This phenomena is induced by the flat wall and is well known [77, 37].

To quantify the layered structure we measure the time-averaged number density for the large particles $n(z)$. This is shown in Fig. 2.2 for smooth (a) and rough (b) boundaries. We set $z = 0$ at the center of the particle whose center is closest to the boundary. The vertical dotted lines indicate the separate layers. As the sample is composed of two sizes of particles, the layer structure decreases rapidly away from

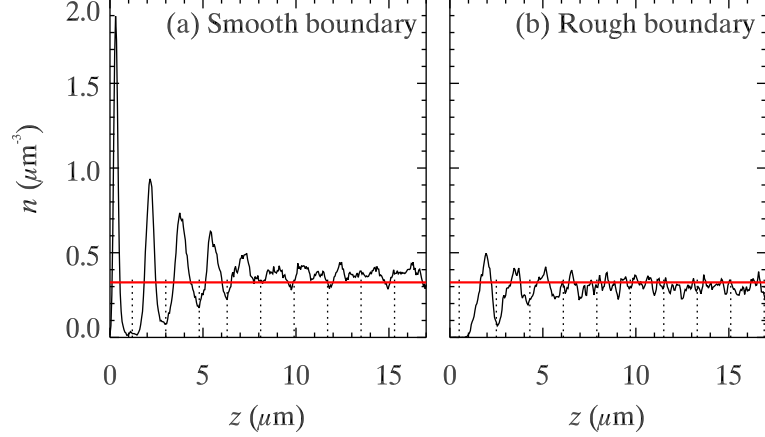


Figure 2.2: The local number density $n(z)$ as a function of the distance from the boundary at $z = 0 \mu\text{m}$ for samples near (a) a smooth boundary and (b) a rough boundary. Layer-like structures are observed in both samples in first few layers, although they are sharper for the smooth boundary and persist to larger z . The vertical dotted lines indicate separate layers, with a fixed spacing once the layers become ill-defined. The red horizontal lines show the average number density in the region $z > 10 \mu\text{m}$.

the wall, consistent with simulations [71, 97] and experiments.[37] The first peak in Fig. 2.2(a) has the maximum value and minimum width, indicating particles are in a well-defined layer, consistent with Fig. 2.1(a). By the sixth layer, it is unclear if there is still a layer or if we are seeing random number density fluctuations. For the rough wall in panel (b), the layers become poorly defined by the fourth layer. For later analysis, we continue counting the layers by defining them in the bulk region to be every $1.8 \mu\text{m}$ based on the typical spacing of the well-defined layers. Note that for the rough boundary condition, the wall texture occupies some of the space of the first layer, thus decreasing the number of dark purple particles in Fig. 2.1(b) and reducing the area under the first peak in Fig. 2.2(b).

Aging manifests as a slow change of sample behavior with increasing t_{age} , where the rate of change slows at longer times[142]. The easiest quantity to see this with our data is the mean square displacement (MSD) of particle motion [85, 163]. Fig. 2.3 shows the motion parallel to the boundaries for (a,b) rough and (c,d) smooth boundaries, with panels (b) and (d) corresponding to the bulk MSD curves. The different colors

indicate different ages. The mean square displacement is computed as $\frac{1}{2}\langle\Delta x^2 + \Delta y^2\rangle$ where the angle brackets indicate an average over all large particles and over all starting times within the window of t_{age} . For our shortest time scale ($\Delta t = 1$ min) the MSD curves have a shallow slope indicating particles are trapped by the local configuration, with the exception of the black curves ($t_{\text{age}} \leq 8$ min) when the aging has just started. At long time scales, the MSDs show an upturn, which is related to the samples' age [26, 85, 163]. For larger t_{age} the lag time particles need to reach the same MSD increases, indicating the slowing particle motion. Note that as we take data, the fluorescent dye in the particles begins to photobleach and our particle tracking resolution worsens, slightly increasing the measured MSD values at small Δt [116]. Slight differences in image quality may also be affecting the overall height of the MSD curves between the smooth and rough boundary conditions for the data at $\Delta t \leq 10$ min [116]. Accordingly, for subsequent analysis below, we will focus on large Δt values for which the signal is greater than the photobleaching noise. The main points to learn from Fig. 2.3 are that the overall behavior of the curves shows the expected aging trend with larger t_{age} , and panels (b,d) show the aging curves are similar for both boundary conditions far from the boundary.

Figure 2.3(a) shows the MSD curves for xy motion for the first layer with rough boundary conditions. Surprisingly, there barely exists any differences comparing to Fig. 2.3(b), which depicts the MSDs of the fourth layer. The particles overall show aging behavior with slower dynamics for larger t_{age} . In contrast to the rough boundary, the MSD curves for the first layer next to the smooth boundary look strikingly different from the bulk case, as seen by comparing Fig. 2.3(c) and (d). In all four time groups the MSD curves in the first layer are slightly smaller than those in the fourth layer. The smooth wall greatly restricts particle mobility, similar to what has been seen for dense colloidal liquids near smooth walls [37]. Moreover, unlike the fourth layer, where the MSD curves strictly follow the aging order, the aging process seems

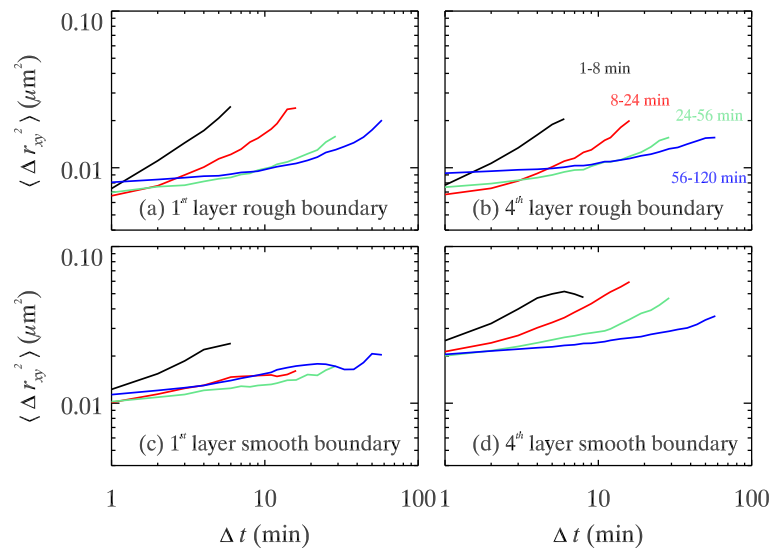


Figure 2.3: The mean square displacement for motion parallel to the boundaries calculated as $\Delta r_{xy}^2 = \frac{1}{2} \langle \Delta x^2 + \Delta y^2 \rangle$. The data are averaged over four different t_{age} regimes as indicated. Data are for (a) 1st layer with a rough boundary, (b) 4th layer with a rough boundary, (c) 1st layer with a smooth boundary, (d) 4th layer with a smooth boundary. The data for the 4th layers match the bulk behavior, and their progression to larger time scales with increasing t_{age} demonstrates that the sample is aging. The data for the 1st layers show that aging is fairly unchanged for the rough boundary (a), but markedly different for the smooth boundary (c).

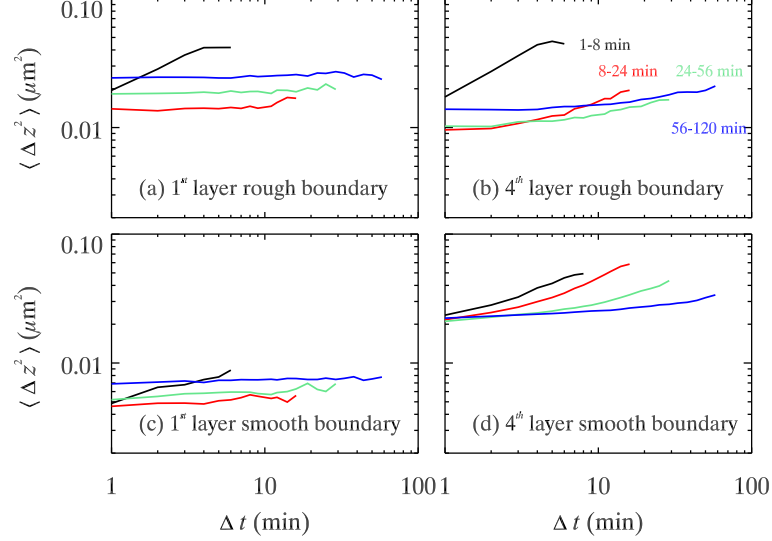


Figure 2.4: The mean square displacement along the direction perpendicular to the boundary (z) calculated during four different t_{age} regimes as indicated. Data are for (a) 1st layer with a rough boundary, (b) 4th layer with a rough boundary, (c) 1st layer with a smooth boundary, (d) 4th layer with a smooth boundary.

to reach a t_{age} -independent state by $t_{\text{age}} = 8$ min. This is likely because the dynamics in this layer are extremely slow, including the aging dynamics. This explanation is also consistent with the pronounced first layer density peak seen in Fig. 2.2(a).

Figure 2.4 shows the MSD data for the z component of motion, perpendicular to the boundary. The results are similar to the MSD data of Fig. 2.3, with the exception that the layers closest to the boundaries show less motion [panels (a,c)] for both rough and smooth boundary conditions. The increase in the height of the MSD curves with age in Fig. 2.4(a,c) is due to photobleaching, but otherwise those MSD curves are fairly flat. Here the first layer for the rough boundary shows some differences with the bulk behavior [compare panels (a) and (b)]. The contrast between first layer and bulk is stronger for the smooth boundary condition [compare panels (c) and (d)].

To better understand the influence of the boundaries, we consider a complementary analysis, examining $\langle \Delta r^2 \rangle$ at a fixed Δt and varying t_{age} . We choose $\Delta t = 20$ min, where Figs. 2.3,2.4 show that the particles' average movement decreases with increasing t_{age} in both smooth and rough boundaries. Figure 2.5 shows the data divided by

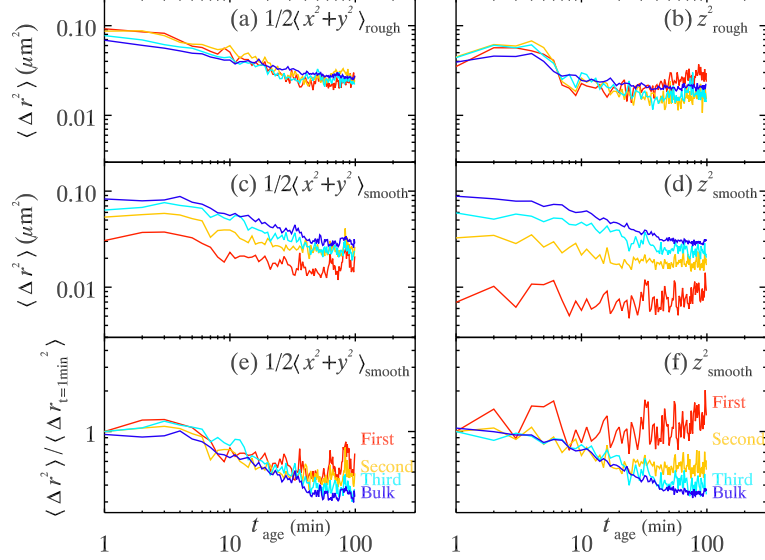


Figure 2.5: Average distance particles move over $\Delta t = 20$ min, as a function of aging time t_{age} . The curve colors indicate the layer number as labeled in panels (e,f). Panels show data for motions parallel to the boundary ($1/2\langle x^2 + y^2 \rangle$) and perpendicular to the boundary ($\langle z^2 \rangle$) for rough and smooth boundaries as indicated. In panels (e,f) the data are normalized by their initial values.

rough boundary condition (panels a,b) and smooth boundary condition (panels c,d), for motion parallel and perpendicular to the boundaries (left and right panels respectively). The colors indicate different layers, as labeled in panels (e,f). The overall decreasing trend of all the curves with larger t_{age} is the signature of aging, with the logarithmic t_{age} axis making apparent that the rate of decrease itself is slower in older samples. The data suggest the sample is still aging at the longest times observed in our experiment, although even reaching a state-steady for $\Delta t = 20$ min does not preclude the sample from still having an aging signal at longer Δt .

For the rough boundaries [Fig. 2.5(a,b)], the data collapse for all layers confirming that the boundary appears to have a negligible influence on the dynamics. However, for the smooth boundary condition, the wall-induced structures bring significant differences for motion parallel to the boundary [Fig. 2.5(c)] and even larger differences in the perpendicular direction [Fig. 2.5(d)]. Both types of motion are slower closer to the wall. For the motion perpendicular to the boundary (panel d), the motion

in the first layer is around ten times smaller than the bulk. Moreover, unlike other layers, we do not observe an aging signal in the first layer – the curve is essentially flat. The lack of observed aging behavior of Δz^2 suggests that this first layer has very slow dynamics. Of course, the perpendicular motion in the first layer is bounded at $z = 0$, but the displacements we observe are much smaller than for the first layer next to the rough wall, which has a similar constraint on perpendicular motion. Our observations of nearly immobile particles with no aging signature in this first layer matches results from thin polymer films near attractive silica substrates [118].

As a different way of understanding how the aging process changes near the smooth boundary, we normalize $\langle \Delta r^2(t) \rangle$ by $\langle \Delta r^2(t_{\text{age}} = 1 \text{ min}) \rangle$ as shown in Fig 2.5(e,f). For both motion parallel and perpendicular to the boundary, the data collapse moderately well for $t_{\text{age}} \lesssim 10 \text{ min}$, indicating an initial aging trend. For $t_{\text{age}} \gtrsim 10 \text{ min}$, the first and second layers nearly stop evolving while the other layers are still aging. This is especially true for the z motion (panel f).

To further explore the relation between the layering structures and motion perpendicular to the boundary we define $\langle \Delta z_{\text{asym}}^2 \rangle$. This is the average of the data of Fig. 2.5(b,d) in the asymptotic regime, that is, for $t_{\text{age}} \geq 85 \text{ min}$. The results are plotted as a function of the distance from the wall in Fig. 2.6(a). The smooth data (red circles) smoothly increases as z increases. The rough data (blue triangles) are fairly constant, with the exception of the first layer ($z = 0.8 \mu\text{m}$) which is larger. As argued above based on the flatness of the data in Fig. 2.4(a), this increase in the first layer is likely due to photobleaching than true motion. For $z > 5 \mu\text{m}$ the differences between smooth and rough data are likely due to image quality which artificially increases the MSD [116]. To account for this, in Fig. 2.6(b) are normalized by the value of $\langle \Delta z^2 \rangle$ averaged over $t_{\text{age}} \leq 5 \text{ min}$. This collapses the data for $z > 5 \mu\text{m}$. These data are related to the amount the dynamics slow as the sample ages, with 1 corresponding to no slowing and smaller values indicating slowing with age. The

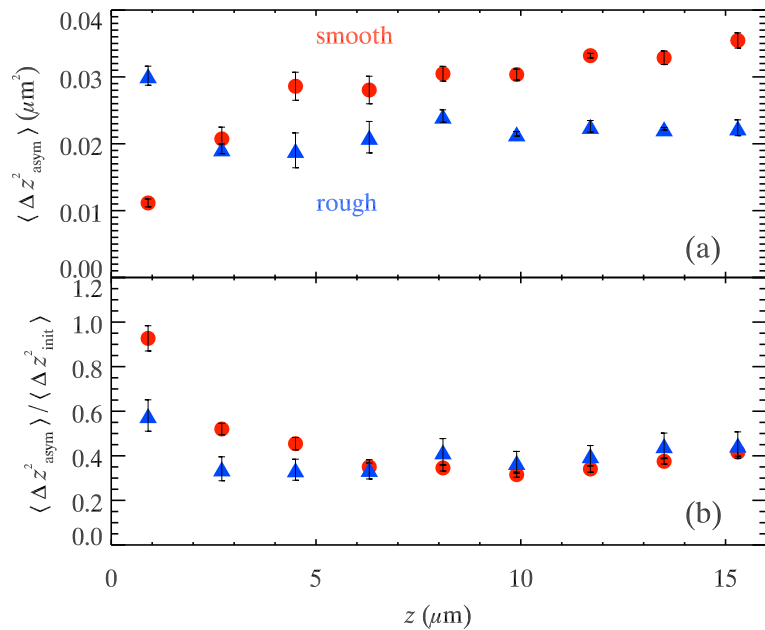


Figure 2.6: (a) The t_{age} average of Δz^2 for the last 15 min of Fig. 2.5(b,d) plotted as a function of z , with the average done over all particles in a layer (as defined in Fig. 2.2). The z value is the center of each layer over which the average is taken. (b) The same data normalized by the mean value of Δz^2 for $t_{\text{age}} \leq 5$ min. This represents the slowing seen due to aging; the data close to 1.0 show little or no aging behavior. The error bars represent the variability in the results when different ranges for the t_{age} -averaging are used.

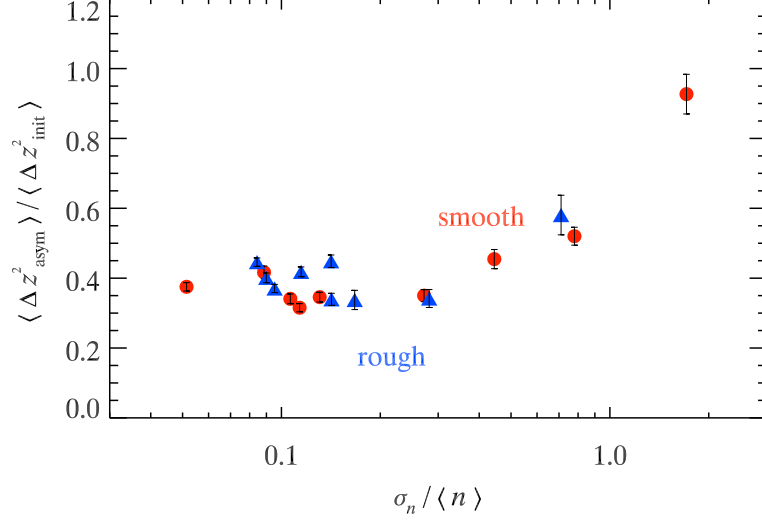


Figure 2.7: The large t_{age} motion in z plotted as a function of the standard deviation of number density σ_n over the mean number density $\langle n \rangle$ where these quantities are defined within each layer (see Fig. 2.2). The data for the vertical coordinate correspond to that of Fig. 2.6(b).

value close to 1 for the smooth boundary condition indicates that the first layer barely ages, consistent with the similarity of the MSD data of Fig. 2.4(c) and the horizontal red line in Fig. 2.5(d). The decrease in the data of Fig. 2.6(b) as z increases shows a return to the normal aging seen in the bulk.

The qualitative similarity of the rough and smooth data in Fig. 2.6(b) motivate an attempt to collapse the data by a horizontal shift. Noting that the number density data of Fig. 2.2(b) look like a horizontally shifted portion of the data of Fig. 2.2(a), we use the local layer structure as a possible way to explain the dynamical data. We quantify the structure using the standard deviation of $n(z)$ within a layer divided by its mean. This nearly collapses the data (to within fluctuations of $\sim 20\%$) accounting for most of the effect. The data for $\sigma_n / \langle n \rangle \lesssim 0.2$ are essentially the bulk region. Thus the difference in dynamics between the smooth and rough boundaries we observe can be explained by the difference in particle layering that occurs next to these two interfaces.

2.4 Conclusions

In our experiment we study aging by observing particle motion in a colloidal glass near smooth and rough boundaries. Both samples exhibit aging in their bulk regions. Near a smooth boundary, the particles form layers against the boundary such that in the two layers closest to the wall, motion is greatly diminished. For a smooth wall, we observe the influence of the boundary extends up to ≈ 6 layers (≈ 4 large particle diameters) into the sample. The observations of a gradient in dynamics near the smooth wall are qualitatively similar to prior observations of gradients near interfaces in glassy materials. Direct evidence for gradients in dynamics has been seen in molecular dynamics simulations [73, 135, 136] and colloidal experiments [132, 65]. In other experiments the influences of the boundaries are inferred from local probes near the boundary (e.g., Ref. [118]) or fitting the data to models assuming boundary effects (e.g., Ref. [120]).

Here we not only see the gradient in dynamics, but observe that this gradient in dynamics is directly related to a gradient in the structural properties. For a rough boundary, the wall-induced structure is greatly reduced and the dynamics appear more bulk-like near the boundary, being similar to that far into the bulk. By comparing the local dynamics near the rough and smooth boundaries, our results suggest that the dominant factor modifying aging dynamics near a boundary is the structure caused by the presence of the boundary. By presenting a rough amorphous boundary, the structure is more bulk-like and thus the dynamics are more bulk-like. A fruitful area for future work would be to explore boundary textures that have intermediate influences on layering structure.

These experimental results on colloidal glasses suggest a viable means by which neutral rough amorphous boundaries may be implemented in computer simulations. This is an issue that computational studies on the influence of interfacial effects on local dynamics have been struggling with for more than two decades [9, 73, 135, 136,

56, 28, 42], and has relevance for the implementation of theoretical point-to-set studies [16, 79, 60, 59]. The method employed in the present study creates a rough amorphous boundary by randomly sticking particles to a smooth wall at approximately 30-50% surface coverage. The local aging dynamics we observe near such a rough boundary appear nearly bulk-like with little deviation from bulk particle densities.

Chapter 3

Random packing of rods in small containers: X-ray tomography experiments

Adapted from JO Freeman, S Peterson, C Cao, Y Wang, SV Franklin, and ER Weeks, *Granular Matter* **21**, 84 (2019)

3.1 Introduction

3.1.1 Random close packing

People have long been curious about how objects pack into containers. Kepler conjectured that spheres pack most efficiently when arranged into hexagonal layers – a supposition that was finally proven in 2005 [52, 53]. There is also the more practical question of inefficiently packed objects (e.g. sand or grain filling a container). At the highest packing densities that are still disordered, this is termed random close packing, although mathematically this is an ill-defined concept [145]. Experimental studies have long recognized the influence of finite-sized and boundary effects on the

packing [21, 3, 125, 138, 164]. It was pointed out in the 1940's that one can extrapolate the observed packing density in containers of various sizes to infinitely large containers [154, 19, 137]; early reports noted that particles pack less efficiently in small containers.

Later work investigated how the boundaries modify the particle packing. Particles can form layers against the wall; for monodisperse packings, these layers can persist rather far from the boundaries [125, 138, 77]. A more recent investigation by Desmond and Weeks used simulations to study the packing of bidisperse random close packed samples [30]. They considered a 2-phase model in which packed particles are treated as a core region packed to the infinite-container volume fraction ϕ_∞ surrounded by boundary layer of thickness δL packed at $\phi_\infty + \delta\phi$. This was an extension of a prior model that assumed δL was the diameter of a particle. Desmond and Weeks found evidence that δL was indeed of order the diameter of a particle, and $\delta\phi < 0$: that is, the sample packed poorly against the boundaries.

In this chapter we probe the packing of rods in small containers. We focus on containers larger than the rod length; containers with dimensions smaller than that would force rods to align simply to enter the container [167]. We are curious about how boundary layers affect the orientation and pack efficiency of rods. We further investigate the boundary layer properties using x-ray tomography, confirming that the layers are thin, about half a rod length. The tomography results reveal that the bottom boundary layer, top boundary layer, and side boundary layer are all distinct. We then conduct experiments with different boundary conditions and further explore how boundary layers affect packing's structure.

3.1.2 Recent studies on long thin packing

Studies of how long thin particles pack have a long history, including experiments using wooden rods [96, 167, 115], plastic rods [106, 98, 141, 143, 29], spaghetti [112,

84], colloidal silica particles [115, 129], glass fibers [41], iron rods [102], lead cylinders [12], and metal wires [45, 115, 121]. Simulations have also been done with a variety of methods [40, 25, 160, 2, 49, 68, 43, 166]. The efficiency of such packings has relevance for nanocomposites (mixtures of polymer resin and fibers) [96, 41, 70], ceramics [96], and filtration and catalysis [45, 25, 98]. As noted by Williams and Philipse [160], these studies agree fairly well on the dependence of the close packing volume fraction ϕ_{rcp} on aspect ratio α ($\phi_{\text{rcp}} \sim 1/\alpha$, for long rods with $\alpha \gg 1$). This widespread agreement suggests that geometry plays a larger role in determining packing than the physical properties of the particles.

Most studies used large containers to minimize the influences of boundaries. A few noted container size dependence: Dixon studied boundary effects on aspect ratio 1 cylinders (equal height and diameter), which pack less efficiently in small containers, albeit with a reversal when the container diameter approaches the particle size. For cylindrical containers of moderate radius R and large height, he found that $\phi(R)$ was well described by a second-order polynomial in $1/R$, but his study was only of the aspect ratio 1 particles. Zhang *et al.* also studied the packing of aspect ratio 1 particles, using x-ray tomography to observe the structure near the container walls [164]. A key result was that the volume fraction within two particle diameters of the wall was lower than that of the bulk. Zou and Yu [167] investigated the packing of rods with aspect ratios 1-64 in cylindrical containers. Their results suggested the existence of a critical container size: for a container of large enough radius R and height H , the results became independent of the container size. They also found that rods packed less densely in smaller containers. Tangri *et al.* reported [143] that aspect ratio 5.35 rods packed at lower ϕ in smaller containers and that cylindrical containers of diameter larger than 5 particle lengths reached the large container limit. Desmond and Franklin [29] observed that rods poured in smaller containing cylinders exhibit solid-body resistance to an intruder; Trepanier and Franklin [146] observed

similar preparation-dependent solid-body behavior in free-standing rod-piles once the confining container was removed. Benyahia [12] observed oscillations in the volume fraction near container walls for rods with aspect ratio 1, 2, and 3.

Desmond and Weeks [30] developed a model (building on [154, 19]) to understand the finite size effects of packing particles in a container. The model assumes a boundary layer of thickness δL with a packing fraction that differs from that found in the bulk (ϕ_∞) by $\delta\phi$. Applying this to a cylindrical container (radius R , height H) one can differentiate between the bulk volume

$$\begin{aligned} V_{\text{bulk}} &= \pi(R - \delta L)^2(H - 2\delta L) \\ &\approx V - \pi\delta L(2RH + 2R^2) \end{aligned} \quad (3.1)$$

which packs at ϕ_∞ and the surface volume

$$\begin{aligned} V_{\text{surf}} &= V - V_{\text{bulk}} \\ &\approx \pi\delta L(2RH + 2R^2) \end{aligned} \quad (3.2)$$

which packs at $\phi_\infty + \delta\phi$. (Terms of order δL^2 and higher are neglected in these definitions.) The net volume fraction ϕ is a volume-weighted sum of the two regions:

$$\phi = [V_{\text{bulk}}\phi_\infty + V_{\text{surf}}(\phi_\infty + \delta\phi)]/V \quad (3.3)$$

which can be shown to reduce to:

$$\phi(R, H) \approx \phi_\infty \left[1 + 2 \frac{\delta L}{L} \frac{\delta\phi}{\phi_\infty} \left(\frac{L}{R} + \frac{L}{H} \right) \right]. \quad (3.4)$$

Equation 3.4 suggests that a plot of packing fraction ϕ against a dimensionless inverse container size $L/R + L/H$ will result in a straight line with a y -intercept at

the bulk/infinite-container size packing fraction ϕ_∞ and a slope $2\frac{\delta L}{L}\frac{\delta\phi}{\phi_\infty}$ that quantifies the impact of the boundary layer. While the slope does not uniquely determine $\delta L/L$ or $\delta\phi/\phi_\infty$, as we will show below x-ray tomography and the detailed information contained in simulations do allow for independent determination of these parameters. While Desmond and Weeks dealt with an isotropic pile with no difference between top, bottom and side boundaries, their model is easily generalized to account for boundary layers of differing characteristics.

3.2 Experimental details

3.2.1 Rods and CT scanners

Julian Freeman from our group first conduct a series of experiments with two different height ($H_{tall} = 12.8$ cm and $H_{short} = 7.4$ cm), and different diameters ranging from $2R = 0.63$ cm to 12.62 cm. Different aspect ratio (from 4 to 32) and glass beads are employed in our experiments (see more details in JO Freeman et al, Granular Matter 21, 84 (2019)). In this dissertation, we will focus on 3D x-ray tomography experiments. We conducted several x-ray tomography experiments to capture the three-dimensional structural information on our rod packings; see Fig. 3.1. These are done with our hand-cut aspect ratio 8 acrylic rods (0.32 mm diameter, length $L = 2.57$ cm). These experiments were done with only two specific cylindrical containers, a large one with $2R = 5L = 12.62$ cm and a smaller one with $2R = 1.9L = 4.48$ cm, both with height $H = 2.9L = 7.4$ cm. For each packing we gently pour the particles into the container until the container overflows. Different than what Julian did, rods are not removed from the top [46]. The filled container is scanned with a computed tomography scanner, RealTime-2722 (UEG Medical Imaging Equip Co. Ltd). It is a specifically designed CT scanner for teeth, with 0.2mm resolution and high scanning speed (less than 10s per scanning). We repeated the experiments five times for each

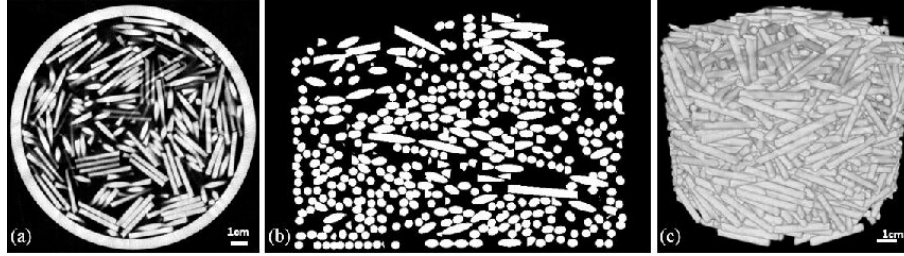


Figure 3.1: X-ray tomography data of rods with length $L = 2.57$ cm, aspect ratio 8 in a container with $R = 13.2$ cm $\approx 5.2L$ and $H = 7.4$ cm $\approx 2.9L$. (a) X-ray image showing horizontal cross section through the container. (b) Vertical cross section, where the white voxels are those above a threshold intensity. The smallest white dots are the corners of rods. (c) 3D rendering of the tomography data.

container, for a total of ten three-dimensional tomography images.

3.2.2 Image processing

We use MATLAB as our image processing tool. There are four main steps we take in order to segment and reconstruct rods' packing: First, we remove the thickness of the container. Since the container is slightly tilted, we start with determining the central axis by finding centroids in each slide. After that, to remove the bottom part, we then construct a surface perpendicular to the central axis at the height when the rods first show up and remove all the pixels that below the surface. Similarly, to remove the side part, for each slide we determine its centroid and radius r , and remove all the pixels whose distance to the centroid is larger than r ; second, we exploit binarization and watershed segmentation to obtain rods' center and orientation \vec{L} [165]. To do that, we manually set an intensity threshold, above which are rods and will have an intensity=1, on the contrary below which is background and have an intensity=0. After obtaining the binary image, we employ watershed (a built-in algorithm in MATLAB) method to find the edge of each rod, in this way we can segment 95% of the total rods, see figure 3.2 (a),(b); third, as an additional analysis step, we arbitrarily choose a height near the top of the container as an artificial top

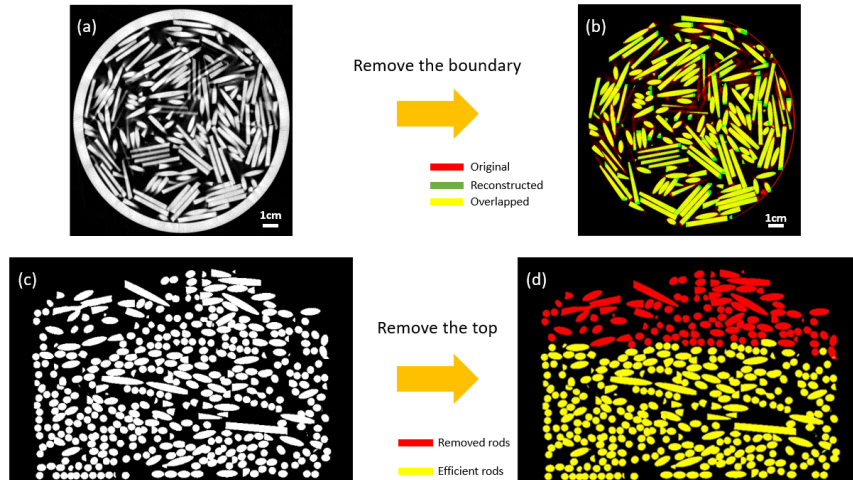


Figure 3.2: We take four steps to obtain the reconstructed packing: We remove container's boundary and segment the rods from (a) to (b); we then reconstruct the packing and set a 'fake' top boundary from (c) to (d).

container boundary (in our experiment $z=300$ pixels, 60 mm). We remove all rods which have any portion above this artificial boundary. In this way, the reconstructed packing is similar to the bulk measurements where rods were removed by hand, but additionally avoiding any disturbance of the remaining rods due to vibrations when removing rods, or also remaining rods which might settle if a removed rod was helping support them in their original position; At last, we reconstruct the whole packing to calculate the volume fraction ϕ . In more details, for each rod, according to its centroid and orientation, we replot the rod and define the intensity within the rods to 1. We then slightly expand/decrease the size of reconstructed rods by comparing it with original scanning images, see figure 3.2 (c),(d).

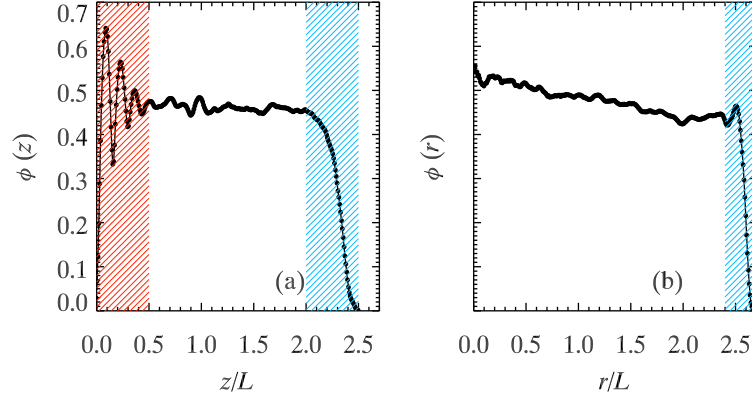


Figure 3.3: (a) Volume fraction $\phi(z)$ as a function of distance z from the bottom boundary and (b) volume fraction $\phi(r)$ as a function of distance r away from the central axis. These data correspond to a short wide container with diameter $2R \approx 4.9L$ and height $H \approx 2.9L$. In figure (a), the red and blue shaded regions represent the top and bottom boundary layers, with boundary thickness of $\delta L = 0.5L$ (estimated by eye). In figure (b), the blue shaded area represents the side boundary layer, with a smaller boundary thickness $\delta L = 0.3L$ (again estimated by eye). Both z and r are normalized by rod's length L .

3.3 3D rods results

3.3.1 Tomography results

The x-ray tomography data sets, while limited to aspect ratio $\alpha = 8$ rods, allow us to probe the volume fraction locally at every position in the container and directly look for boundary effects. In Figs. 3.3(a) and 3.4(a), we plot the local volume fraction $\phi(z)$ as a function of vertical position z , averaged over all particles with radial positions $r < R - 0.3L$, so as to exclude from consideration any radial boundary effects. Likewise in Figs. 3.3(b) and 3.4(b) we plot $\phi(r)$ averaging over only particles with z at least $L/2$ away from both the bottom and top container boundary. Thus, in each case, $\phi(z), \phi(r) \approx \phi_\infty = 0.467 \pm 0.002$ in the middle of the container by construction.

We estimate the thickness of the top layer to again be $\delta L = L/2$, as indicated by the blue shaded regions of Figs. 3.3(a) and 3.4(a). Here the rods are quite loosely packed, with $\delta\phi_T/\phi_\infty = -0.39$ [Fig. 3.3(a)] and $\delta\phi_T/\phi_\infty = -0.48$ [Fig. 3.4(a)]. The magnitude of the reduced volume fraction make sense given our protocol for treating

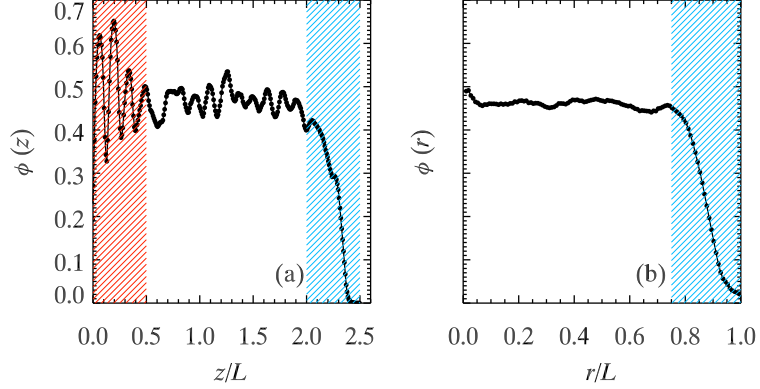


Figure 3.4: (a) $\phi(z)$ as a function of distance z away from the bottom boundary and (b) $\phi(r)$ as a function of distance r away from the central axis. These data correspond to a short narrow container with diameter $2R \approx 1.9L$ and height $H \approx 2.9L$. All three boundary layers have the same thickness as the data shown in Fig. 3.3, as well as the same bulk value of ϕ_∞ .

the top boundary of the x-ray data, where we remove rods overlapping our arbitrarily defined top boundary. In the end, roughly half of those rods will be removed. These results are also in good agreement with theoretical arguments from Yaman *et al.* [162] which found $\delta L = L/2$ based on geometric arguments, and $\delta\phi/\phi_\infty = 1/2$ near a flat wall.

At the bottom of the containers [red highlighted regions of Figs. 3.3(a) and 3.4(b)], there are distinct layer structures. The spacing of these layers corresponds to the rod diameters ($L/8$ in this case), suggesting that the bottom-most layer of rods lies flat against the flat bottom boundary. The reduction in amplitude of the fluctuations of $\phi(z)$ is due to the subsequent layers of rods lying at slight angles and packing more randomly above the flat bottom layer. These layers are evidence of the symmetry breaking of gravity and our filling procedure. By eye, the fluctuations appear to decay within $L/2$ from the bottom [the red shaded regions in Figs. 3.3(a) and 3.4(a)], consistent with prior experiments of Montillet and Le Coq [98]. Interestingly, although rods in the red shaded region of Figs. 3.3(a) and 3.4(a) are layered, the mean volume fraction in this region is nearly the same as the bulk region: the fractional change in ϕ is only $\delta\phi/\phi_\infty = +0.01$.

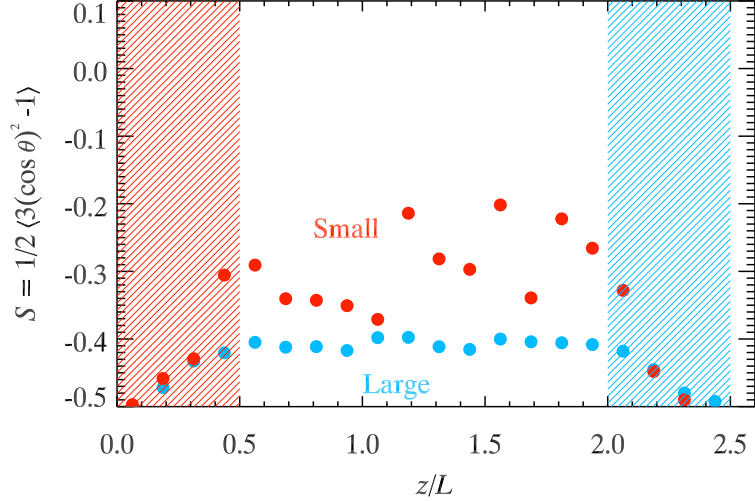


Figure 3.5: Nematic order parameter S as a function of vertical position z/L for the large ($2R = 4.9L$) and small ($2R = 2.9L$) containers as indicated. $S = -1/2$ corresponds to horizontally aligned rods, and $S = 0$ corresponds to isotropically oriented rods.

X-ray tomography reveals that the side boundaries [Figs. 3.3(b) and 3.4(b)] are thinner. We estimate their thickness to be $\delta L = 0.3L$, as indicated by the shaded regions in those graphs. Within those regions, the volume fraction is changed by $\delta\phi/\phi_\infty = -0.25$ for the larger diameter container, and -0.27 for the smaller diameter container.

Simulations, which do not incorporate gravity, show an isotropic distribution of rods. X-ray tomography allows us to study the experimental orientation distribution and, in particular, how it changes near the boundaries. We use the nematic order parameter $S \equiv (1/2)\langle 3\cos^2\theta - 1 \rangle$, where $\theta \in [0, \pi/2]$ is the angle with respect to the vertical axis. $S = 1$ corresponds to perfectly vertically aligned rods, and $S = 0$ corresponds to the case of isotropically oriented rods. Fig. 3.5 shows the intriguing result $S < 0$ for all regions in the sample, with $S \rightarrow -1/2$ near the bottom and top of the container. As argued above, the data of Figs. 3.3(a) and 3.4(a) near $z = 0$ indicate horizontally oriented rods lying in a flat layer on the bottom of the container. For such rods, $\theta = \pi/2$ and $S = -1/2$. At the top of the container, while the rods are

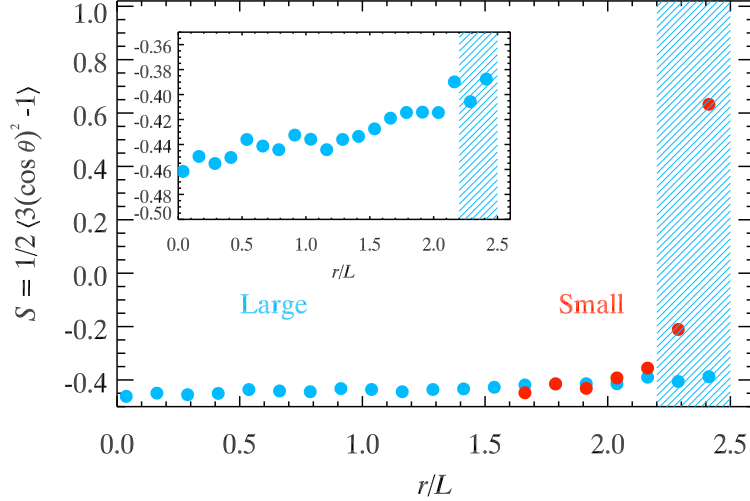


Figure 3.6: The nematic order parameter S as a function of the distance r/L away from the center axis. The blue shaded region represents the side boundary layer; compare with Figs. 3.3(b) and 3.4(b). The inset graph is an expanded view of the large container data.

not in strictly flat layers, nonetheless for a rod center to be close to $z = H$ requires the rod to be nearly horizontal, so again at the top $S \rightarrow -1/2$ makes sense. In the middle of the container, S increases toward zero but does not reach it. This indicates that the rods are somewhat more randomly oriented, but still are influenced by gravity; they still are more horizontal than not. Indeed, this can be directly seen in the x-ray images of Fig. 3.1(b,c), and also seen in an earlier 3D visualization experiment with aspect ratio 5 rods [98].

We additionally examine S as a function of radial distance r/L , shown in Fig. 3.6. Here the smaller container data (red) are shifted horizontally so that the boundary layers overlap for the two data sets. For the smaller container data, S approaches 1 right at the container boundary, showing that the vertical container walls strongly align the rods with the vertical. This makes sense, as the curvature of the container boundary prevents the center of a horizontal rod from coming closer than $0.09L$ to the container wall; for a rod center to be at the container wall, the rod must be vertically aligned. This effect is diminished for the larger diameter container, for which

curvature matters less; see the inset of Fig. 3.6. Prior work showed that vibrating containers of rods results in alignment of the rods [155, 161], with the alignment starting near the boundary [48]. Our observations suggest that some small amount of ordering is already present near the walls prior to any vibrations.

We briefly return to Fig. 3.3(b), which shows a slight increase in $\phi(r)$ near the center of the container ($r \rightarrow 0$). We do not know why this occurs, nor is this behavior seen in the smaller container [Fig. 3.4(b)]. However, it is consistent with the orientational behavior shown in the inset to Fig. 3.6, where the rods at the center of the container are more horizontal (S closer to $-1/2$) than those farther from the center. Presumably in the center of the container, the more horizontally aligned rods pack slightly better.

3.3.2 Implications of tomography data on bulk parameters

Julian Freeman in this bulk experiment also observed that gravity breaks the symmetry between horizontal and vertical boundaries. As a result, the simple model Eq. 3.4 is no longer applicable and must be generalized to account for the different boundary effects. Each of these boundaries has its own independent thickness $\delta L/L$ and volume fraction perturbation $\delta\phi/\phi_\infty$. The derivation of Eqn. 3.4 can be repeated, leading to a new model for $\phi(R, H)$:

$$\phi(R, H) \approx \phi_\infty \left[1 + 2C_R \left(\frac{L}{R} \right) + (C_T + C_B) \left(\frac{L}{H} \right) \right] \quad (3.5)$$

with

$$C_R = \frac{\delta L_R}{L} \frac{\delta\phi_R}{\phi_\infty}, C_T = \frac{\delta L_T}{L} \frac{\delta\phi_T}{\phi_\infty}, C_B = \frac{\delta L_B}{L} \frac{\delta\phi_B}{\phi_\infty}. \quad (3.6)$$

The C terms describe the boundary packing effect of the radial, top, and bottom boundaries respectively[46]. In Julian's experiment, by varying container's radius with a fixed height, he obtained C_R by fitting ϕ with corresponding L/R for rods

aspect ratio ranging from 4 to 32. He also varied containers' height to obtain $C_T + C_B$ vice versa.

Our tomography results for $\alpha = 8$ can be summarized as $C_R = -0.078$, $C_T \approx -0.22$, and $C_B = 0.005$. We can now make inferences about our model parameters based on the x-ray results. The magnitude of the product $[|C_R| = (\delta L_R/L)(|\delta\phi_R/\phi_\infty|)]$ is $\sim 0.05 - 0.1$ [46]: this suggests that either the thickness of the boundary layer is small, or the decrease in volume fraction within the boundary layer is small, or both. From the x-ray data we have $\delta L_R/L \approx 1/3$ for $\alpha = 8$ rods. Assuming this is similar for other aspect ratio rods, we infer $\delta\phi/\phi_\infty \approx -0.15$ to -0.30 for much of Julian's data.

For the top boundary layer, the x-ray data suggest $\delta L_T/L \approx 1/2$, $\delta\phi_T/\phi_\infty \approx -1/2$, so $C_T \approx -1/4$. (More precisely, $C_T = -0.22$ for the $\alpha = 8$ rods from the x-ray data, but that's more precision than needed at this point when considering other aspect ratio rods for which we have no direct x-ray data.) Turning to the bottom layer, for the cases with $C_B + C_T \approx 0$, assuming $\delta L_B/L \approx 1/2$, this then suggests $\delta\phi_B/\phi_\infty \approx +1/2$. For $\alpha = 20$ we have $C_B + C_T \approx 0.65$ and for $\alpha = 24$ we have $C_B + C_T \approx 0.80$. Assuming the top layer has $C_T \approx -1/4$ still, it suggests these aspect ratio rods have an unusually thick or dense bottom layer. The layering seen in Figs. 3.3(a) and 3.4(a) for small z has a periodicity related to the rod diameter, suggesting that the thickness of the bottom boundary layer may be more due to the rod diameter rather than rod length: thus the thickness may be 4 rod diameters, which happens to be $L/2$ for the $\alpha = 8$ rods but would be smaller for larger aspect ratio rods. If this is true ($\delta L_B/L$ smaller for longer aspect ratio rods) then $\delta\phi_B/\phi_\infty$ could be larger than 1 for the $\alpha = 20, 24$ rods. This is certainly possible as $\phi_\infty \approx 0.2$ for these rods, leaving plenty of empty volume to potentially be packed more efficiently at the bottom of the container. Indeed, prior simulations showed that a quasi-2D layer of randomly packed rods will pack to a higher volume fraction than the same rods packed randomly in

3D due to the likelihood of 2D rods to locally align [40]. A nearly quasi-2D layer can pack even more densely [40].

3.3.3 Comparison with simulation data

Sean Peterson and Scott Franklin from RIT conducted the 3D rod simulations and compare them with our results [46]. Simulations allow us to investigate the boundary layer direction and confirm that, in the absence of gravity, there are no substantive differences in packing near the horizontal and vertical boundaries. Moreover, when ϕ is normalized by ϕ_∞ and plotted as a function of r/L or z/L , the data for different aspect ratio rods collapse. Figure 3.7 shows the data for the local packing fraction averaged over all different aspect ratios as a function of distance from the horizontal and vertical boundary. The two curves are within statistical uncertainty and reasonably well fit by a stretched exponential. Visually Fig. 3.7 suggests a boundary length of about $0.25L$, consistent with that seen in tomography data for the sidewalls [Figs. 3.3(b) and 3.4(b)]. We note that this is independent of particle aspect ratio, suggesting a purely geometric effect.

Tomography experiments revealed the importance of gravitational-induced layering, which begins at the bottom boundary but persists throughout the bulk of the pile. In particular, the nematic order parameter $S \equiv \frac{1}{2}(3\langle \cos^2 \theta \rangle - 1)$ does not asymptote to zero as one would expect for a random distribution of particle angle (Fig. 3.5). In simulations the situation is quite different. Fig. 3.8 shows the nematic order parameter as a function of distance from the nearest boundary. Rods near the boundary are aligned with boundary, as they must be, but this rapidly decays to zero. Once particles are more than half a rod-length from the side they are no longer constrained and isotropically sample the full angular space.

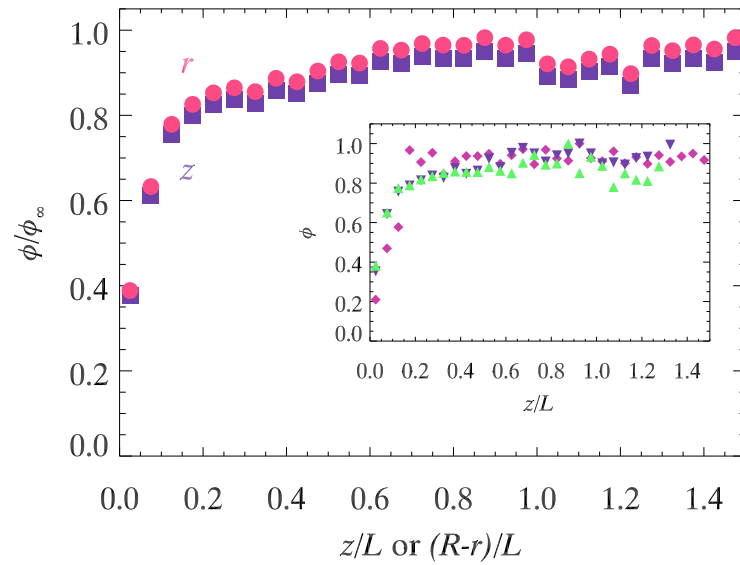


Figure 3.7: Local packing fraction ϕ/ϕ_∞ as a function of distance from the nearest boundary, averaged over all aspect ratios from the simulation data. The circles are as a function of $R - r$, and the squares are as a function of z . Inset: Data from specific aspect ratios $\alpha = 4$ (light violet diamonds), 16 (green upward triangles), and 32 (dark violet downward triangles).

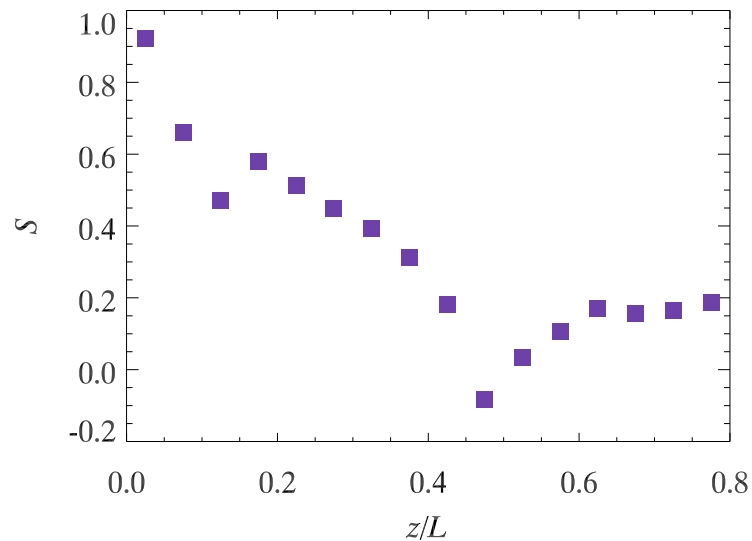


Figure 3.8: Nematic order parameter as a function of distance from the top or bottom boundary, from the simulation data averaged over aspect ratios 4 and 12.

3.3.4 Discussion

It has been known that long thin particles pack poorly when packed randomly [40, 115, 167, 160, 141]. Our results show that randomly packed long particles pack even more poorly in smaller containers. X-ray tomography experiments and bulk packing data demonstrate the existence of three types of boundary layers: a dense bottom layer where rods lie flat, and loosely packed side and top boundary layers. This behavior is captured by a generalization of a previously derived model that divides the space into a bulk and a boundary region, each with their own distinct volume fractions. Our modification incorporates the difference between bottom and top/side boundaries observed in experiment.

The bottom layer is clearly due to gravity and our packing protocol. Simulations without gravitational effects reveal more purely geometrical boundary layers of loosely packed particles. Interestingly, while nematic order parameter in computationally generated piles indicates an isotropic distribution of rod orientation, the boundary layer thickness is less than half a rod length and comparable to those found in experimental data. This finding that the boundary layer is thinner than that suggested by purely geometric constraints is the most significant result from all of our data, experimental and computational. For all but the most constraining containers, then, the impact of the boundary on the overall volume fraction, while measurable, is generally small.

3.4 2D and Sandpaper

3.4.1 2D rods packing results

After we explore the boundary layer in 3D, we are curious about investigating how boundary affects rods' structure in 2D. Julian Freeman designed a fancy experimental

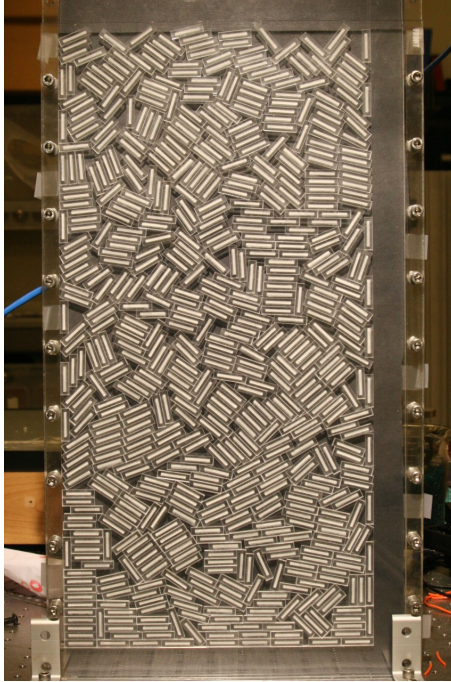


Figure 3.9: 2D experimental set-up, designed by JO Freeman

set-up see in Fig. 3.9, which allows us to take high-quality images. We use laser-cut rectangles for imaging, with 1:4 aspect ratio. Noticeably there are more alignments in 2D packing, which makes it more difficult to segment rods apart. To solve that, we have a laser-frosted white rectangle on rods to enhance the contrast between edge and bulk area, see Fig. 3.9.

Since volume fraction ϕ is not comparable in 2D and 3D, the question we are most curious about is how the rods' orientation change when they are near the bottom/side boundary in 2D. Here we set gravitational direction as y axis, and define $y = 0$ at the bottom edge. The farther it is away from the bottom edge, the larger y it would be. Similarly we set another direction as x axis, as x increase from left edge to right edge.

We still use the nematic order parameter $S \equiv (1/2)\langle 3 \cos^2 \theta - 1 \rangle$ in figure 3.5 , where $\theta \in [0, \pi/2]$ is the angle with respect to the vertical axis. $S = 1$ corresponds to perfectly vertically aligned rods, and $S = 0$ corresponds to the case of isotropically

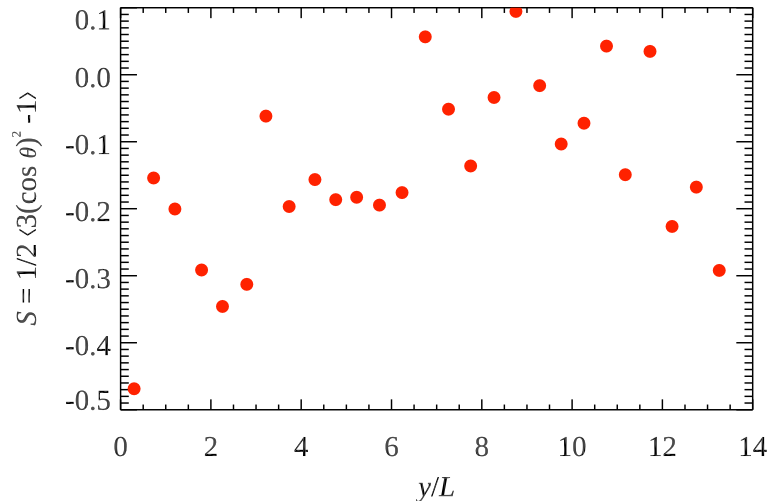


Figure 3.10: Nematic order parameter S as a function of vertical position y/L for 2d packing. $S = -1/2$ corresponds to horizontally aligned rods, and $S = 0$ corresponds to isotropically oriented rods.

oriented rods. Fig. 3.10 shows consistent results with 3.5: $S < 0$ for all regions in the sample, with $S \rightarrow -1/2$ near the bottom and top of the container. Interestingly, rods are more randomly distributed in the bulk area, compared with 3D packing.

Figure 3.11 shows that near the side boundary in 2D packing, rods are almost perfectly vertically aligned, this may be related to cluster structures in 2D packing. More results are waiting to be explored in future projects.

3.4.2 Sandpaper results

Jason Jiang introduces smooth and rough boundary conditions to 3D rod packings by attaching smooth/rough sandpapers to container's inner wall. We still use hand-cut acrylic rods with aspect ratio 1:8. We employ two different sandpapers: Coated Abrasives Manufacturing Institute (CAMI) 60 for least fine abrasive (diameter range from 40.5 to 58.5 μm) and CAMI 15k for most delicate abrasives (diameter range from 8.4-12.6 μm). We follow the same procedure (see details in Rods and Scanners session) to pour rods into our container, see figure 3.12. We collaborate with Prof

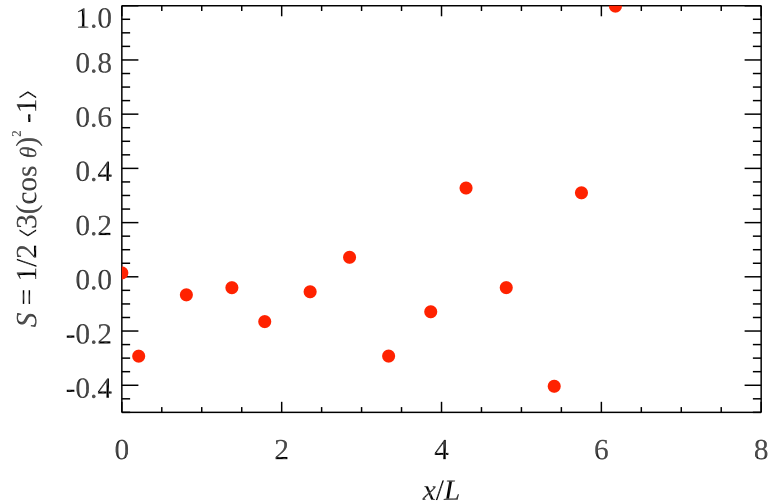


Figure 3.11: The nematic order parameter S as a function of the distance x/L away from the boundary.

Amir Pourmorteza and scan our packings with CT scanner in Emory hospital. For each packing we repeat the process 5 times to reduce experimental error.

From figure 3.13 we can still observe layer-like structure near the bottom boundary, as we observe in figure 3.3. Smooth boundary condition (15k) seems to have a higher volume fraction ϕ in bulk area than rough boundary (60grit).

We also take a look at how side layer will affect the volume fraction ϕ . The most interesting result here is that rough boundary tend to have a thicker boundary layer than the smooth one. We estimate their thickness to be $\delta L = 0.3L$ for 15k sand paper, and $\delta L = 0.5L$ for 60 grit sand paper, as indicated by the shaded regions in those graphs. More boundary conditions and local structure characteristics are waiting to be explored in future projects.

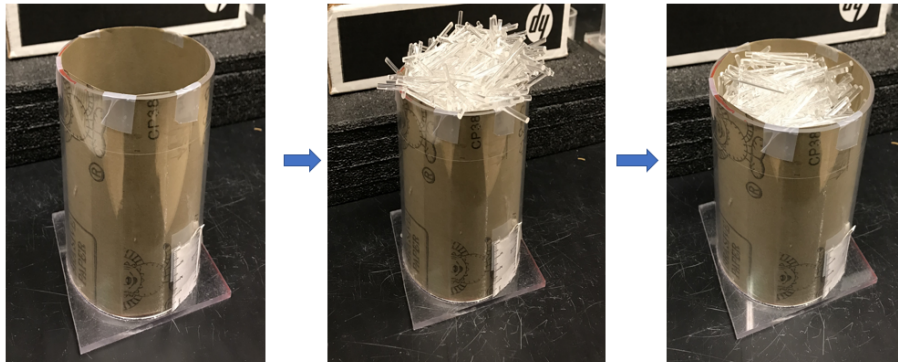


Figure 3.12: We pour rods into containers with sandpaper (from left to right): First, we attach sandpaper to container's inner wall; Second, we pour rods gently into containers; Last, we remove rods on top gently.

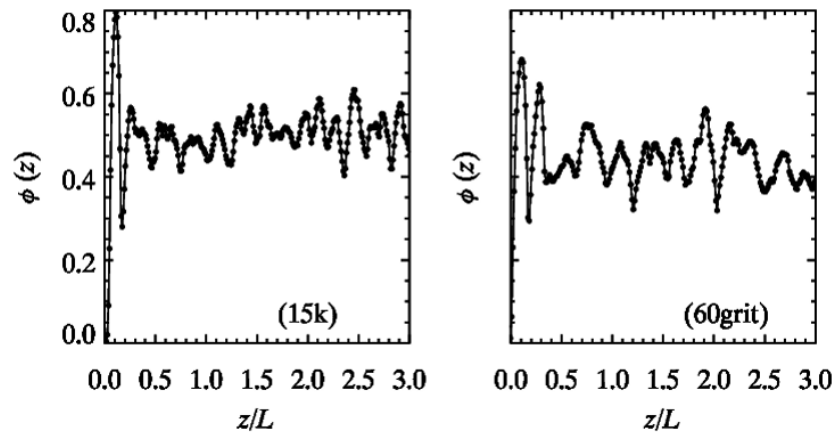


Figure 3.13: Volume fraction $\phi(z)$ as a function of distance z from the bottom boundary for both smooth (15k) and rough boundary condition (60grit).

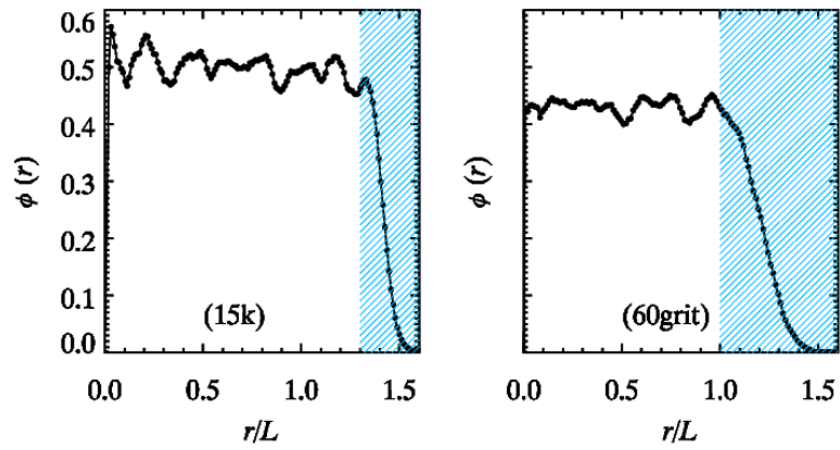


Figure 3.14: Volume fraction $\phi(r)$ as a function of distance r away from the central axis with smooth boundary condition (15k) and rough boundary condition (60grit).

Chapter 4

Rheology of jammed and glassy materials

4.1 Introduction

Soft amorphous solids include granular materials, foams, and pastes. These are solid in the sense that they possess a yield stress: they elastically (reversibly) support a finite stress below the yield stress, and deform irreversibly if the applied stress exceeds the yield stress [17]. In particular, these materials can typically support their own weight: you can make a pile of sand, a pile of shaving cream, or a pile of paste. A granular material such as sand is comprised of solid particles, typically mm or larger sized. A colloidal paste is made from solid particles in a liquid, typically μm size or smaller (small enough to undergo Brownian motion). Foams are gas bubbles in a liquid, stabilized by surfactant molecules to prevent the bubbles from coalescing, and typically with mm or larger sized bubbles. Another soft amorphous solid can be found in emulsions: these are composed of liquid droplets in another immiscible liquid, again with surfactant molecules needed for stabilization, and with droplet sizes ranging from 10 nm up to a few hundred μm [92]. In all of these examples,

by diluting the particles the material can lose its solid-like properties: for example, adding water to a pile of shaving cream will eventually change the pile of foam into a puddle with bubbles. More technically, the yield stress for these materials is a function of the volume fraction ϕ : as the fraction of particles in the volume is decreased, the material flows easily. For $\phi > \phi_c$, the yield stress becomes nonzero, with ϕ_c depending on details of the system. When these materials undergo the transition from liquid-like to solid-like behavior, these materials share some similarities with glass transition, another situation where a liquid can be changed into an apparent solid [81].

Previously Liu, Nagel, and coworkers [81, 107, 82] presented the jamming framework to unify these transitions from liquid into solid. They suggested that in order to change a jammed system into an unjammed one, there are three possible options: increasing the temperature, decreasing the volume fraction, and increasing the applied stress above the yield stress. This can be restated as a conjecture that the yield stress is a universal function of temperature and volume fraction. Focusing just on particulate systems such as the ones mentioned above, one would expect that granular materials, foams, colloids, and emulsions would share a common ϕ_c (at least if their particle size distributions are equivalent [31]). However, it has long been noted that the “colloidal glass transition” happens at $\phi_g = 0.58$ [119, 64], and random close packing of granular particles happens at $\phi_{rcp} = 0.63$ [13] (both situations considering essentially monodisperse hard particles). For an emulsion, a 1995 rheology experiment by Mason, Bibette, and Weitz noted that there was evidence of solid-like behavior for $\phi \geq \phi_g$, and then onset of a higher modulus for $\phi \geq \phi_{RCP}$ [90]. The discrepancy in ϕ_c was directly addressed in simulations [66], which showed that instead of extrapolating into each other, the colloidal glass transition at ϕ_g and the jamming transition at ϕ_{RCP} are distinct. The rationale is that systems with larger particles are athermal, and thus have a jamming transition, whereas systems with smaller particles are thermal and see a glass transition. For samples of intermediate particle

size, two transitions may be possible. Ref. [66] predicted that such phenomena can be observed by measuring rheological performances of dense emulsion samples from 1 - 10 μm [66]. Indeed, the 1995 emulsion results of Ref. [90] support this prediction qualitatively, using droplets with mean diameter $d = 1.00 \mu\text{m}$. Overall, the thinking is that a thermal system will have a glass transition at the lower volume fraction ϕ_g , but that the particles do not need to touch until they reach the higher volume fraction ϕ_{RCP} . For $\phi > \phi_{RCP}$, particles must deform, which is straightforward for emulsion droplets, so the rheological behavior for these large volume fractions must be dominated by the physics of the particle deformation (for example, surface tension effects for deformed emulsion droplets). In contrast for $\phi < \phi_{RCP}$ the rheology is determined by the thermally driven glass transition, for suitably thermal particles or droplets.

A series of experiments have explored the possibility of two distinct transitions, using emulsions [134, 111, 33, 34] and colloidal systems [10, 157, 105, 113]. Most experiments focus on rheological measurements since the yield stress can be easily obtained from a plot of stress as a function of strain [95]. Work done primarily at the University of Pennsylvania studied thermosensitive PNIPAM colloidal particles [10, 105]. These samples allow for the volume fraction to be adjusted by changing the temperature. In the second of these two papers (Basu *et al.* [10]), they measured the rheological behavior of several samples and compared with their earlier results (Nordstrom *et al.* [105]). Between the two papers, the particle diameters ranged from 0.4 to 1.4 μm , to potentially cover both thermal and athermal sizes; however, the large particles used in the earlier study were softer than the smaller particles used in the later study [10]. The small particle samples exhibited a glass transition with $\phi_c = 0.61 \pm 0.02$, while the large particle samples had a jamming transition with $\phi_J = 0.635 \pm 0.003$. For these samples, because the volume fraction changed are due to particle size changes (controlled by temperature), the influence of thermal

fluctuations changes by nearly a factor of two from smallest to largest volume fractions studied. Their experiments also used somewhat large steps in volume fraction (≈ 0.01 in Ref. [105], ≈ 0.05 in Ref. [10]), making it challenging to precisely identify the transition points in the latter work.

In the recent work of Dinkgreve *et al.* [34], they study rheological behaviors of athermal emulsions (diameter $3.2 \mu\text{m}$) and compare with earlier published emulsion data [91] (diameters $0.5\text{-}1.5 \mu\text{m}$) and earlier colloid data (diameter $0.37 \mu\text{m}$). The athermal samples had a yield stress for $\phi > \phi_J \approx 0.64$, and the smaller particle samples all had yield stresses for $\phi > \phi_g \approx 0.58$. Nonetheless, they found all samples had similar scaling of their rheological curves, independent of where their transition to a yield stress was found. However, the large and small emulsion samples used different oils, so it was difficult to directly compare the rheological data.

In this work we measure rheological behavior for both monodisperse and bidisperse dense emulsions with droplet diameters ranging from $1\text{-}2 \mu\text{m}$. We create our emulsions by using the TPM (3-(Trimethoxysilyl)propyl methacrylate) seed-growth technique [149]. We consistently use a weighing method to measure our samples' volume fractions. We observe a yield stress appears above $\phi_g = 0.58$ for our samples with smaller droplet diameters ($d \approx 1 \mu\text{m}$) and at $\phi_J = 0.63$ for our sample with the largest droplet diameter ($d \approx 2 \mu\text{m}$). Using one type of emulsion (TPM oil) and changing the volume fraction while maintaining a constant droplet size enables us to directly compare samples with identical properties apart from volume fractions; and to compare results of droplets with different diameters but otherwise identical composition. Our results show that indeed two distinct transitions can be seen. Furthermore, we find that a bidisperse sample composed of both small and large droplets has comparable rheological behavior to samples composed only of small droplets.

4.2 Experimental details

4.2.1 Sample synthesis

In order to prepare monodisperse samples ranging from several hundred nanometers to several micrometers, we tried three different methods: fractionation [14], swelling method [148], and seed growth method [149]. Fractionation method was first introduced by Prof. Bibette in 1992. There are mainly four steps: first, pre-mix the sample; second, dilute the sample with low concentration SDS solvent and gather the floating creamy; third, add more SDS and gathered the upper creams; fourth, repeat above three steps and combine samples with same SDS concentration. To start with, we pre-mixed the silicone oil and water with 0.2 % wt SDS by ultrasonifier, in this way a polydisperse sample with particles' diameters ranging from dozens of nanometer to several hundred micrometer can be obtained. After that, we dilute the pre-mixed emulsion 10 times with 0.2 % SDS solvent, after the solution sit still for a day or so, due to the depletion force, the upper cream can be separated from the dilute bottom phase. Then we add 0.1 % wt more SDS into the dilute forms, wait one day, again save the upper cream and add more surfactant till it reach 0.8 %. For cream we collected, they are rather monodisperse emulsions with around 0.5 volume fraction (the floating speed is determined by particle size). To further narrow down particles' size distribution, for each cream we repeat the whole process and mix cream obtained from the same SDS concentration together. In this way, monodisperse emulsions can be obtained see Fig. 4.1. However, when we conducted this method, we found that sample's size range heavily relies on pre-mixed samples. In our trial, we can only obtain emulsions around 2 μm . The other disadvantage of this method is that it's very time-consuming, usually it takes about two weeks to finish a whole cycle, and it usually produces no more than 10 ml effective samples at one time (barely enough for one rheological experiment).

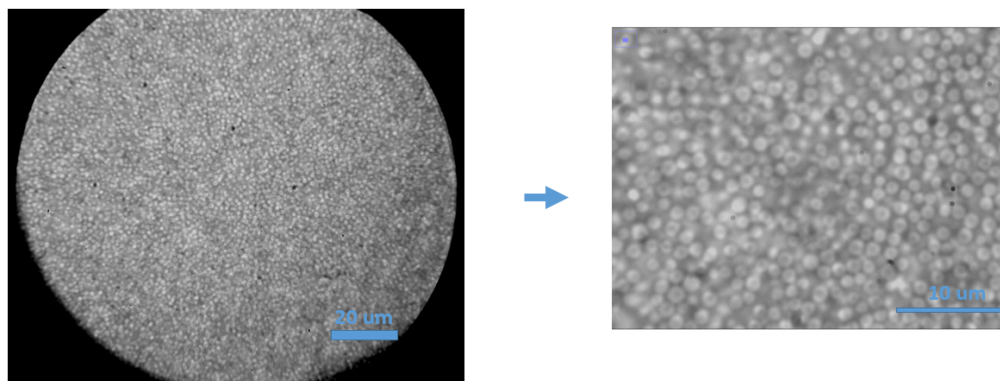


Figure 4.1: Monodisperse emulsions (silicone oil + water) obtained by fractionation methods, the mean diameter is around $2 \mu\text{m}$. Image was taken by Leica DM IRB research microscope.

We also tried swelling method [148]. In short, we take a $2 \mu\text{m}$ monodisperse polystyrene latex (Bangs lab), add to it a 0.2 wt% SDS solution, then add a solvent for polystyrene like toluene, xylene, or chlorobenzene (here we use toluene). We then use slow magnetic stirring for 3-4 hours, then let the excess solvent float to the top and remove. The amount of swelling will be determined by the size of the original particles – the smaller the particle, the less it swells volumetrically. In our experiment, the swelled emulsion increase its diameter by around three times, see figure 4.2. If you don't want to have a charged surfactant for your system, you might have to play around with some nonionic surfactants. Overall we can control emulsions' sizes excellently by changing polystyrene particles with a low polydispersity. The biggest drawback of this method is that it's too expensive. To produce 10 ml samples, it takes at least 1000 dollars to achieve our goal. The other drawback of this method is that toluene is easy to evaporate, it requires extreme caution to conduct the rheological experiments, since shear stress measured is sensitive to sample's evaporation, especially in low shear rate regime.

At last, we choose to employ the seed growth method. To prepare our TPM samples, we use a seeded-growth method [149] to obtain TPM emulsions at required

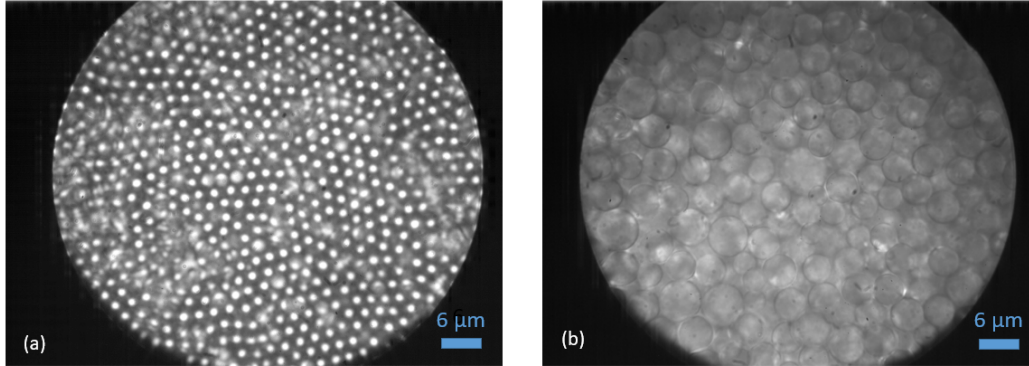


Figure 4.2: (a), Polystyrene particles ($d=2\ \mu\text{m}$) observed under Leica DM IRB research microscope. (b) swelled emulsions observed under same conditions (average diameter is around $6\ \mu\text{m}$).

size. First we add 1 ml (2 ml for larger emulsions) TPM oil (3-(Trimethoxysilyl)propyl methacrylate 98 %, Sigma-Aldrich) into 100 ml pre-made ammonia solution (1 ml 2.8% ammonia diluted with distilled water at least 100 times) in a sealed plastic beaker with a stir bar. We use a pH meter to determine the ammonia solution's pH before we injected TPM oil since it would react with glassware [149]. Usually the appropriate pH lies in between 10-12, the higher the pH, the smaller the droplets are. When pH is lower than 10, large polydisperse samples (range from 2-50 μm) are observed. We first stir the solution at a high speed (rpm=350) to hydrolyze the oil for 20 minutes, then lower the rpm to 200 to condense oil monomers. After that every hour we add additional 1 ml TPM until droplets grew to our desired size. When it comes to produce large emulsions, 100 ml additional solvent will be added after fifth time injection in order to prevent the oil-water phase separation (usually happens when $\phi_{\text{tpm}} > 0.05$). By tuning ammonia solution's pH and ϕ_{tpm} we can produce 10 ml emulsion droplets with diameters ranging from 800 nm to 2.1 μm with a low polydispersity at one time; see Fig. 4.3. We then add 0.5 wt% F108 (Synperonic F108 from Sigma-Aldrich) and 5 mM sodium chloride to stabilize our samples. Surfactant and salt concentration can be adjusted depending on your

experiments: 0.05 wt% F108 is good enough to stabilize emulsions and conducting microscopy experiments, but may lead to clusters when samples undergo high-speed centrifuge; salt concentration can also be played around to change potential energy between emulsions, in our experiments we stick with 5 mM sodium chloride after several trials.

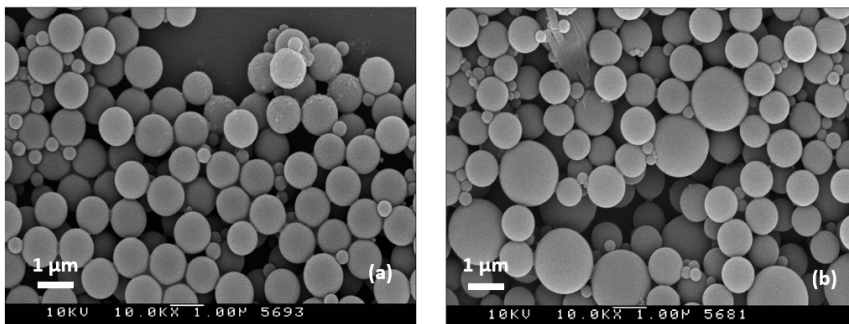


Figure 4.3: TPM emulsions polymerized by AIBN and observed under SEM (a) Monodisperse sample with $d_{\text{mean}}=1.16 \mu\text{m}$ (b) Bidisperse sample with diameter $d_{\text{small}}=1.06 \mu\text{m}$, $d_{\text{large}}=1.86 \mu\text{m}$. Sub-nano particles were only observed after polymerization and may be due to unreacted TPM oil.

4.2.2 Measuring volume fraction

We first obtain a concentrated stock emulsion by centrifuging our initial samples several times. We use Eppendorf Centrifuge 5702 and perform the centrifuge for 60-90 minutes at 4000 rpm. Sometimes transparent lump will be observed after the centrifuge process. This suggests that something went wrong during the sample synthesis process and cannot be used in rheological tests. After centrifuge, a series of samples with lower volume fractions are then made by diluting portions of the initial samples with 0.5 wt% F108 and 5 mM sodium chloride in water. To accurately measure volume fraction, each sample is weighted before and after the evaporation of water [116] to determine ϕ_w . Since TPM oil itself can barely evaporate in room temperature (770 times slower than water), it's reasonable to neglect uncertainty brought by TPM evaporation. As in prior work with the same surfactant (Ref. [91]),

we correct our volume fractions to take into account the thickness $h = 17.5$ nm of the water film between two droplets pressed together near ϕ_c . This adjusts the volume fraction as $\phi \approx \phi_w(1 + 3h/2a)$ using the measured ϕ_w and droplet radius a ; these are the volume fractions reported subsequently in this chapter. Note that we use Ref. [91]’s value for h ; we do not have an independent measurement of this value.

4.2.3 Measuring particles’ size

Since our goal is to determine how thermal motion will affect the transition behavior, it’s essential for us to accurately measure emulsions’ size. Here we employ two different methods: differential dynamic microscopy (DDM) and scanning electronic microscope (SEM), and eventually choose SEM to determine our particles’ size.

We conduct differential dynamic microscopy (DDM) method to measure emulsion droplets’ size indirectly [11]. We employ our Leica microscope to take bright-field movies and use MATLAB code provided by the Helgeson lab, UCSB. Simply speaking, we transverse our bright-field movie into Fourier space and measure the intensity fluctuation brought by Brownian motion. In this way, the diffusion constant D can be estimated, and particle size can be calculated through Einstein-Stokes equation. This method doesn’t require high image quality and can work with tiny emulsions (around 10 nm). The drawback of DDM method is that it’s hard to determine samples’ polydispersity (in our experiment it’s one of the most essential factors), although previous research claimed they could predict protein clusters’ polydispersity through second-order fitting [130].

SEM method requires samples to be solid. To accurately measure the sizes of our particles and observe them in real space, we polymerize (turn liquid droplet into solids) a small portion of each sample by adding 90 μL solution into preheated 100 mL 0.1wt % 2, 2-Azobis(2-methylpropionitrile) (AIBN) solution and leave it in a 80 $^{\circ}C$ oven for at least 2 hours[149]. We then observe polymerized sample under SEM

(Topcon DS-150F Field Emission SEM). To assure the successful rate of polymerization process, there are two things worth noticing: first, do not add surfactant before the polymerization process. By adding surfactant will stop AIBN from emulsifying particles, and eventually lead to bad SEM images; second, samples need to be put into the oven immediately after the stirring process. Emulsion samples can last no longer than 3-6 hours without adding any surfactant based on my observation. Polymerization after 6 hours (once stop stirring) usually would fail and cluster-like particles will be observed under SEM. Previous studies suggested that particles' volume will shrink around 7% after polymerization [149]. Sub-200 nm objects were observed only after polymerization and are potentially due to incompletely reacted TPM [149]. These results are consistent with previous prediction [83]. Our droplets are slightly polydisperse: 6-8 %; we do not ever observe our droplets to organize into crystalline arrays. Number we obtained from DDM methods are within 5 % differences than the SEM results. We choose to use the precise sizes measured by SEM as opposed to the more directly measured, but far less precise DDM results. The fact that the diameters we obtained from DDM and SEM method are similar to each other is also consistent with previous research [83].

4.2.4 Rheological details

Our rheological experiments are conducted using an Anton Paar MC502 rheometer. We study three monodisperse emulsions ($d_{\text{mean}} = 1.03, 1.16, \text{ and } 2.04 \mu\text{m}$) and one bidisperse sample ($d_{\text{small}} = 1.06 \mu\text{m}, d_{\text{large}} = 1.86 \mu\text{m}$, with small droplets have same volume with large droplets). For each sample, we perform a steady shear measurement with a 50 mm cone-in-plate geometry (truncation height $53 \mu\text{m}$). A solvent trap is used at side to prevent sample from evaporation. A rough bottom plate is also adopted to eliminate any slip condition. To provide a reproducible initial condition, we pre-shear all samples with a 10 s^{-1} shear rate for 30 s and then sit still for another

30 s. All measurements are performed under room temperature. Sedimentation and creaming of particles is almost negligible within our experimental time scale.

4.3 Analysis and results

Figure 4.4 shows rheological curves for 2.04 μm monodisperse sample, 1.16 μm monodisperse sample and 1.06/1.86 μm bidisperse sample. For all three samples, steady shear measurements are performed from 10^2 /s to 10^{-3} /s shear rate in order to cover a broad range of shear regime. Yield stress σ_y is observed for samples above ϕ_c and is decreasing with ϕ , which is consistent with previous experiments [90, 34, 17].

The curves of Fig. 4.4(a,b) show that the transition from solid to liquid happens at different ϕ for these two different monodisperse samples. For our large droplet sample ($d_{\text{mean}} = 2.04 \mu\text{m}$), $\phi = 0.643$ has a yield stress and $\phi = 0.627$ does not, indicating that the transition volume fraction ϕ_c lies between these two values. This $\phi_c = 0.635 \pm 0.008$ is similar to results observed in granular systems [18]. For our smaller droplet sample ($d_{\text{mean}} = 1.16 \mu\text{m}$), the data indicate $\phi_c < 0.575 \approx \phi_g$, suggesting that this sample is glassy for $\phi \geq 0.575$. Prior work argued that it is hard to accurately compare volume fractions measured by employing different methods [116], and we note that all of our volume fractions likely have an absolute uncertainty of ± 0.03 ; however, the key point is that we use a consistent weight-measuring method for all of our samples, and the relative uncertainties of our stated volume fraction values is ± 0.003 . In some prior work, due to differing volume fraction measurement techniques, the uncertainty for ϕ_c between different groups was as much as $0.58 \leq \phi_c \leq 0.64$ [116]. Here since we use a consistent method for determining ϕ , we have strong evidence that the solid-to-liquid transition occurs at lower volume fraction for the smaller particles. This supports the idea that smaller droplets have more significant thermal fluctuations, resulting in a glass transition at a lower volume fraction, whereas the larger droplets are more

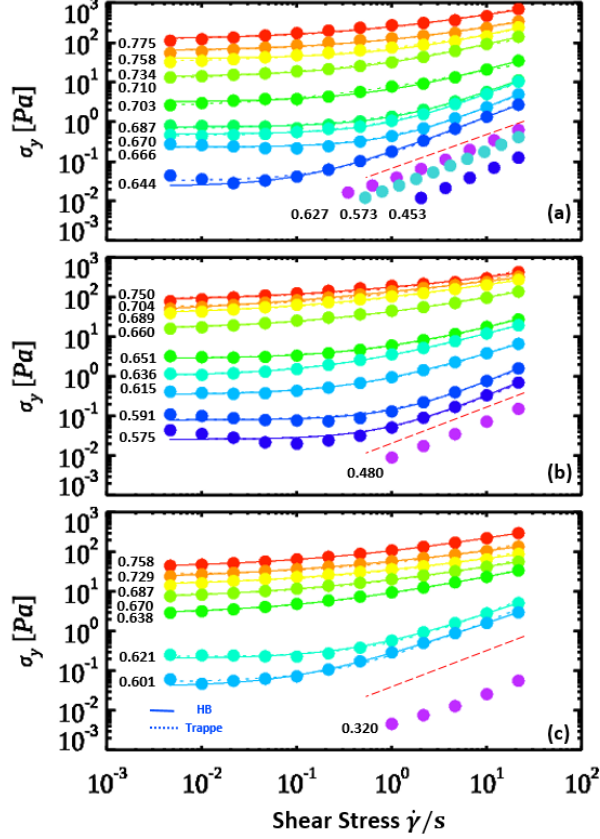


Figure 4.4: Shear stress σ_y plotted as a function of strain rate $\dot{\gamma}$ for (a) $2.04\mu\text{m}$ monodisperse sample, (b) $1.16\mu\text{m}$ monodisperse sample, (c) $1.06/1.86\mu\text{m}$ bidisperse sample. The rheological curves are labeled by their volume fractions ϕ . The solid lines are fitting curves with Herschel-Bulkley model, and the dotted lines are fitting with TC model [20]. The red dashed lines are guidelines that identify the transition between samples with and without a yield stress.

athermal [66].

All data above ϕ_c can be fit well with Herschel - Bulkley model:

$$\sigma = \sigma_y + k\dot{\gamma}^n. \quad (4.1)$$

The scaling factor n is plotted as a function of volume fraction ϕ in figure 4.5 (a),(b). For all samples, n remains rather steady at high volume fraction ($\phi > 0.64$ for $1.16\mu\text{m}$ sample and $\phi > 0.70$ for $2.03\mu\text{m}$ sample), and then start increasing rapidly when further decreasing volume fraction.

We also try to fit our data with TC model[20] in figure 4.4.

$$\sigma = \sigma_y + \sigma_y(\dot{\gamma}/\dot{\gamma}_c)^{1/2} + \eta_{b_g}\dot{\gamma}. \quad (4.2)$$

σ_y is TC model's yield stress, representing for the elastic behavior; $\dot{\gamma}_c$ is the intersection between plastic behavior and elastic behavior, when $\dot{\gamma} > \dot{\gamma}_c$, plastic behavior will dominate system's behavior; η_{b_g} physically means solution's background viscosity and determines the viscous behavior, although the fitting value is much larger than our solvent's viscosity ($\eta = 1.5 * 10^{-3} Pa \cdot s$), as well as TPM's viscosity ($\eta = 2.0 * 10^{-3} Pa \cdot s$ from Thermofisher data sheet). Figure 4.4 shows that for both samples, TC model and HB model fit well with our original data, with less than 10% difference in fitting error. We plot its fitting parameters in figure 4.5. For 1.16 μm sample, we notice that before jamming transition ($\phi > 0.64$), η_{b_g} can almost be neglected, which suggests that viscous behavior play little role in high volume fraction. The abrupt change in η_{b_g} around 0.65 may be related to jamming transition. Similarly we observe a abrupt transition when plotting $\dot{\gamma}_c$ as a function of ϕ , $\dot{\gamma}_c$ goes up to infinity when volume fraction $\phi < 0.61$. When $0.65 > \phi > 0.61$, plastic and viscous behavior coexist and both contribute to sample's rheology performance. For 2.03 μm sample, we also observe those abrupt change in $\dot{\gamma}_c$ and η_{b_g} . Interestingly, in large samples, those change happen at around same volume fraction ϕ , suggesting there is no plastic-viscous co-existing phase for large samples. By comparing HB and TC model's fitting parameters, we notice that both models suggest plastic behavior dominates at high volume fraction (n maintains around 0.5 & $\eta_{b_g} = 0$) and viscous behavior plays a more important role when it's close to glass transition (n quickly increases to 1 & $\dot{\gamma}_c$ goes to ∞).

Since we observe no distinct differences between yield stress obtained by HB and TC model, for simplicity, we will use yield stress σ_y (lines in Fig. 4.4) obtained from

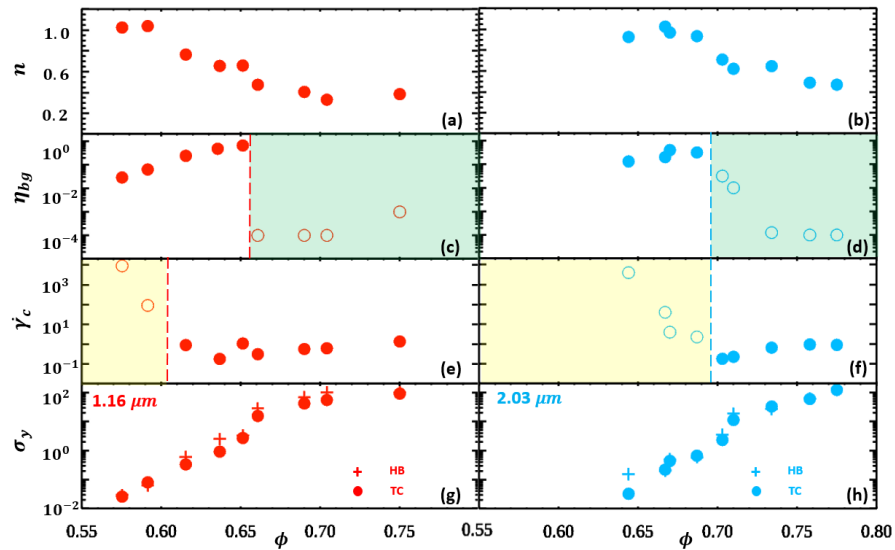


Figure 4.5: The HB and TC model fitting parameters as a function of volume fraction ϕ for 1.16/2.03 μm samples: n as a function of ϕ for (a) 1.16 μm sample, (b) 2.03 μm sample; η_{bg} as a function of ϕ for (c) 1.16 μm sample, (d) 2.03 μm sample. Green shadow region represents that when fit $\eta_{bg}=0$, it would only have less than 1 % difference in fitting error than best fitting parameter; $\dot{\gamma}_c$ as a function of ϕ for (e) 1.16 μm sample, (f) 2.03 μm sample. Yellow shadow region represents that when fit $\dot{\gamma}_c = \infty$, it would only have less than 1 % difference in fitting error than best fitting parameter; σ_y as a function of ϕ (g) 1.16 μm sample, (h) 2.03 μm sample. Filled circles are σ_y from TC model, and + signs are σ_y from HB model, most of the time there are no obvious difference between two fittings.

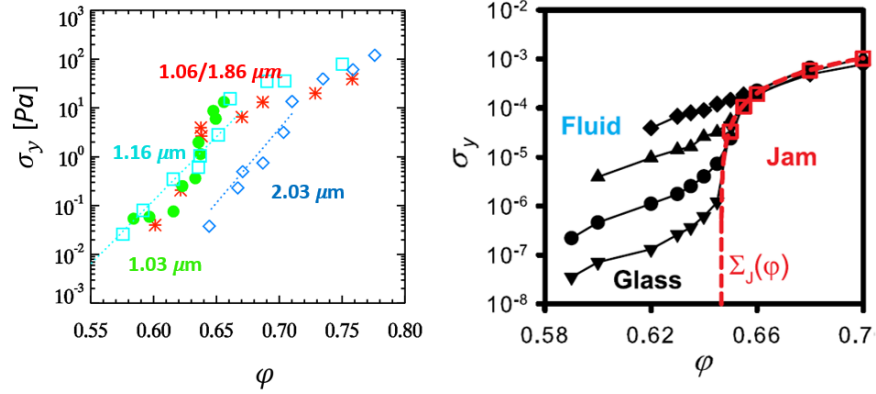


Figure 4.6: (a) The yield stress σ_y as a function of volume fraction ϕ for our experimental data; each set of data is labeled by the mean droplet diameter. The red asterisk data are for the bidisperse sample, labeled by the two mean droplet diameters. The effective temperature ranges from $T_{\text{eff}} = 5 \times 10^{-6}$ for the $d = 1.03 \mu\text{m}$ sample to 1.3×10^{-6} for the $d = 2.03 \mu\text{m}$ sample; see text for details. The dashed lines are exponential fit curves $\sigma_y = \sigma_0 e^{C\phi}$ with $\sigma_0 = 3 \times 10^{-17}$ Pa, $C = 60$ for small particles and $\sigma_0 = 2 \times 10^{-21}$ Pa, $C = 70$ for the larger particles.[74], σ_0 is a fitting parameter with no deep physical meaning behind. (b) Simulation results from Ref. [66]. As ϕ is decreased, the system goes through the jamming transition at around 0.64, with an abrupt drop in yield stress. After that, it will stay in a glassy regime, with only a moderate decrease of the yield stress until it reaches the glass transition point $\phi_g \approx 0.58$, at which point the yield stress vanishes [66]. The red dashed line represents the $T = 0$ limit (for large, athermal particles). For the black curves, the effective temperature varies by factors of ten, ranging from the top black curve (“Fluid,” $T_{\text{eff}} = 10^{-4}$ to the bottom black curve (“Glass,” $T_{\text{eff}} = 10^{-7}$).

HB model in following analysis. To compare with the simulation predictions, we then plot σ_y as a function of ϕ for all our samples in Fig. 4.6(a). In our experiment, for the small droplet diameter samples (1.06, 1.13 μm), the yield stress only weakly depends on ϕ for high ϕ . A more significant change in σ_y is seen around $\phi \approx 0.65$, although σ_y still remains nonzero until $\phi \lesssim 0.58$. In contrast, our large diameter droplet sample (2.04 μm) has a yield stress which starts to decrease rapidly at higher volume fraction (at around $\phi \approx 0.70$), and σ_y disappears at $\phi < 0.643$. These results strongly suggest that the critical solid-to-liquid transition happens at different volume fractions depending on particles' size.

This observation was predicted by Ikeda *et al.* in Ref. [66]; their specific prediction is shown in Fig. 4.6(b). The jamming transition was expected to be “athermal” and seen in all samples at $\phi_J \approx 0.64$, the volume fraction corresponding to random close packed samples; this matches our data in Fig. 4.6. The “thermal” glass transition should occur for samples with smaller droplets around $\phi_g \approx 0.58$; this again matches our data in Fig. 4.6. To characterize the difference between “large athermal” and “small thermal” particles, they considered the reduced temperature $T_{\text{eff}} = k_B T / \varepsilon$, where ε represents an energy scale related to the particle stiffness. This reduced temperature characterizes how easy it is for thermal fluctuations to deform particles, thus allowing them to slip past one another. In our experiment, we measure the TPM surface tension using a dropmeter (Dropletlab), the surface tension measured $\Sigma_{\text{TPM}} = 3\text{mN/m}$, which is consistent with previous work [76]. We assume the deformation energy $\varepsilon = \Sigma_{\text{TPM}} d^2 / 4$, which should be the correct order of magnitude. Using this we get $k_B T / \varepsilon = (1.3 - 5.0) \times 10^{-6}$, lying in the crossover regime predicted by the simulation [66]. The main qualitative difference between our results [Fig. 4.6(a)] and the simulation results [Fig. 4.6(b)] is that our large droplet sample depends more strongly on volume fraction for $\phi > \phi_J$: a fairly smooth decrease in ϕ_J by several orders of magnitude is seen as ϕ decreases from 0.77 to 0.65.

Intriguingly, our bidisperse sample with droplet diameters $1.06 \mu\text{m}$ and $1.86 \mu\text{m}$ behave similarly to the two small droplet size monodisperse samples [Fig. 4.6(a)]. This suggests that in a bidisperse sample, the small droplets dominate the rheological behavior.

For samples with $\phi > \phi_c$, we fit the yield stress data to an exponential growth model; see the straight lines in Fig. 4.6(a). These fits are just to the data where the growth of σ_y appears roughly linear on this semilog plot, so $0.58 \leq \phi \leq 0.64$ for the small diameter emulsion sample and $0.64 \leq \phi \leq 0.70$ for the large diameter emulsion sample. In our experiments, the yield stress grows with volume fraction more strongly when increasing particle's diameter, from $\sigma_y \sim 3 \times 10^{-17} e^{60\phi}$ to $\sigma_y \sim 2 \times 10^{-21} e^{70\phi}$. These fits are consistent with the entropic barrier hopping model suggested by Koblelev and Schweizer [74], despite slight differences in the exponent ($\sigma_y \sim e^{40\phi}$ for them). Consistent with their prediction, the larger the particles are, the more abruptly σ_y will decrease with ϕ .

To further understand how the yield stress changes with volume fraction, we consider three additional data sets from prior literature. Two data sets are taken from Mason, Bibette, and Weitz (Ref. [91]) who studied silicon oil in water emulsions using both steady and oscillatory shear. These emulsions were stabilized by sodium dodecyl sulfate (SDS) and employed the fractionation method to produce fairly monodisperse samples with droplet diameters between $0.5 \mu\text{m}$ to $1.5 \mu\text{m}$; the surface tension was $\Sigma = 9.8 \text{ mN/m}$. They investigated the yield stress of their samples. They concluded that their samples had a size-independent transition which they called a glass transition at $\phi = 0.58$. The third data set is from Dinkgreve *et al.* (Ref. [111, 33, 34]) who studied castor oil in water emulsions using steady shear, similar to our experiments. Their samples had a larger mean droplet diameter, $d = 3.2 \mu\text{m}$, and the surface tension was 1.5 mN/m ; the droplet size was intentionally chosen to be in the athermal regime. The large athermal droplets had a liquid-to-solid jamming transition at $\phi = 0.64$.

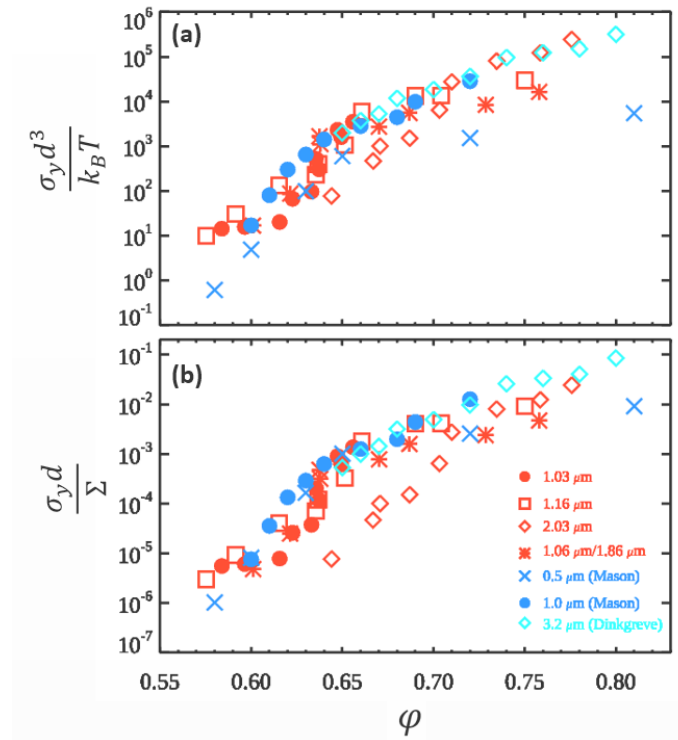


Figure 4.7: (a) The yield stress as a function of ϕ , with yield stress nondimensionalized by the thermal energy $k_B T$. (b) The yield stress as a function of ϕ , with yield stress nondimensionalized by the oil-water surface tension Σ . The legend indicates the droplet diameter d and the source of the data, if not our work.[91, 34]

Intriguingly, in Ref. [34] they also examined the earlier data of Mason, Bibette, and Weitz,[91] and found that all the data (both thermal and athermal droplet sizes) fit well into an identical master curve for $\phi > \phi_c$, albeit with different ϕ_c values for the different droplet sizes.

We compare these prior data sets to our emulsion data Fig. 4.7. To better understand how thermal motion and particle deformation affect our system, here we define a nondimensional thermal yield stress $\sigma_T = \sigma_y d^3 / k_B T$ and a nondimensional mechanical yield stress $\sigma_0 = \sigma_y d / \Sigma$. Our data are the red symbols, and the literature data are the blue symbols, as indicated by the legend in Fig. 4.7(b). In all cases, the reduced temperature is small ($k_B T / \varepsilon \ll 1$). Neither the thermal yield stress [Fig. 4.7(a)] nor the mechanical yield stress [Fig 4.7(b)] collapse the data perfectly. The thermal yield stress comparison is based on a simple idea, that the modulus of a solid should scale as $k_B T / d^3$ for a sample made of components with inter-particle distance d [69] – indeed, this is the basic reason that “soft matter” composed of micron-sized objects is softer than “hard matter” made of atoms with nanometer spacing. This somewhat collapses the data, with the outliers being the smallest diameter droplets ($d = 0.5 \mu\text{m}$ data from Ref. [91]). However, even with our own data, the thermal yield stress varies by an order of magnitude for constant ϕ . In Fig. 4.7(b) we plot the mechanical yield stress; the simple idea here is that the yield stress is due to the surface tension. This is sensible for an emulsion: for fixed $\phi > \phi_c$, approaching the yield stress microscopically means that droplets are pushed into each other, causing them to deform slightly, and thus the surface energy of that deformation gives rise to the macroscopic elastic response. At the yield stress these slight deformations are sufficient to allow droplets to move past one another and the sample can flow. This collapses the data fairly well, with the sole exception being our large droplet sample with $d = 2.03 \mu\text{m}$. It is possible that this is another sign that the large droplet sample has a jamming transition rather than a glass transition, but in that case it is surprising that the still

larger $d = 3.2 \mu\text{m}$ sample from Dinkgreve *et al.* collapses with the smaller droplet data rather than our large droplet data. To summarize Fig. 4.7, it is worth noting that for our own data at least, $k_B T$ and Σ are a constant, so the difference between the two scalings is a factor of d^3 in (a) and d^1 in (b).

Here in our experiments, we successfully cover the droplet sizes in between by using only TPM emulsions and compare both thermal yield stress and mechanical yield stress with Mason's and Dinkgreve's data in figure 4.7. In all systems, reduced temperature $k_B T/\varepsilon \ll 1$, σ_T is well separated with σ_0 . When it comes to thermal shear stress, overall shear motions dominates the emulsions behaviors in the high volume fraction regime. However, when close to transition volume fraction, thermal fluctuation starts to play a more and more important role. In term of mechanical stress, although that we treat ε_{TPM} as $\Sigma_{\text{TPM}} r^2$, energy required to deform emulsion particles should only be differences between original and new ε_{TPM} , thus it may be much less than $\Sigma_{\text{TPM}} r^2$. Based on our calculation, deforming spherical emulsions by 10 % will lead to 0.5 % increase in surface energy. Let's assume Poisson's ratio ν is 0.5 for TPM emulsions due to incompressibility. Before deformation, assume we have a spherical emulsion in order to minimize surface energy. If we extend one axis by Δr , in order to maintain a same volume, the other two axis will compress by approximately $\Delta r/2$. In order to calculate the area differences after deformation, we then obtain that $\Delta A \sim (\Delta r)^2/4$. As a result, our yield stress is actually large enough to deform particles in high volume fraction regime.

In previous experiments, Basu et al [10] and Nordstrom et al [105] studied rheological performances of PNIPAM particles. They employ Young's modulus E and assume particles interact via Hertzian interaction to estimate $\varepsilon_{\text{PNIPAM}}$. Their calculated reduced temperature lies in similar range with us. They did not observe two different transition at the same time. Interestingly, their shear stress changed much less with volume fraction ϕ .

4.4 Conclusion

We have studied the rheological behavior of dense emulsions over a range of droplet sizes and volume fractions, finding evidence of both a thermal-like glass transition at $\phi_g \approx 0.58$ and an athermal-like jamming transition at $\phi_J \approx 0.64$. For the samples with a glass transition, the yield stress becomes nonzero for $\phi > \phi_g$, while for samples without a glass transition, we do not measure a nonzero yield stress until $\phi > \phi_J$. The glass transition is observable in our samples with smaller droplet diameters ($d \approx 1 \mu\text{m}$), whereas our sample with the largest diameter ($d = 2.03 \mu\text{m}$) is the case with only a jamming transition. We additionally find evidence that our samples with a glass transition also have a jamming transition at ϕ_J . This is marked by a dramatic rise of the yield stress by about two orders of magnitude, and also a disappearance of the viscous component from the three-component (TC) model fit (Eq. 4.2). Intriguingly, the “athermal” sample with only a jamming transition shows a transition of a different sort around $\phi \approx 0.70$, where the TC model fit transitions from not having a significant plasticity component ($\phi < 0.70$) to not having a significant viscous component ($\phi > 0.70$). Of course, it is possible that the apparently missing components simply mean that we cannot measure them with the resolution of our rheometer; in particular, the viscous component may simply have moved to shear rates faster than our ability to measure.

The key advantages of our experiments are that we use one type of particle for all measurements, that is, an emulsion droplet, so that the particle interaction does not change as we change the droplet size; we have a consistent means of measuring the volume fraction across all samples; and we vary volume fraction while keeping our droplet size fixed (in contrast to hydrogel particles, for example [10]). A concern might be that we do not have a sample with only a glass transition, and not a jamming transition. However, as per Fig. 4.6(b), our samples have deformable droplets and the volume fraction can always be increased well above ϕ_J , and thus we should always

see a jamming transition around ϕ_J once the droplets begin to deform – which indeed is what is suggested by our data in Fig. 4.6(a).

Prior simulations by Olsson and Teitel found that the rheological curves for soft particles near jamming could be rescaled onto master curves (one curve for jammed samples, a second curve for unjammed samples) [108, 109]. Given that our data are well-fit with both the HB and TC models – but with varying power law exponent n (HB model) or other fitting coefficients (TC model), we have not presented a data collapse of the raw rheological data shown in Fig.4.4. To the extent that the HB and TC models are reasonable fits, the dependence of the fitting parameters on ϕ shows that our data do not follow a master curve. This is in contrast with some prior experimental work with hydrogel particles, for which $n \approx 0.5$ was essentially constant, allowing for a good data collapse.[10, 105] In contrast to our work, these soft hydrogel particles only had one transition (a glass transition) as their volume fraction was increased, even to well above ϕ_{RCP} . The deformability of hydrogel particles is entirely elastic, rather than being due to surface tension as with our emulsion samples. Nonetheless one might expect that at ϕ_g the hydrogel particles would not yet be deformed and that their rheological behavior would change for $\phi > \phi_J$ after deformations are mandatory; this was not seen [10, 105]. Another interesting difference is that our yield stresses increase by three to four orders of magnitude as we increase ϕ (see for example Fig. 4.6), in agreement with the early work of Mason and Weitz [90], whereas the hydrogel particles saw an increase of only one order of magnitude over a similar range of ϕ [10]. Comparing with our work, these interesting differences suggest that liquid-to-solid transitions as the volume fraction is increased may be non-universal in ways beyond the size-dependent glass transition / jamming transition distinction; that the particle type matters as well.

Chapter 5

Conclusion

In this dissertation, we studied soft materials systems covered a broad scale: from $\sim 1 \mu\text{m}$ dense colloids/emulsions to $\sim 3 \text{ mm}$ acrylic rods. We specifically focus on three distinct aspects related to the jamming/glass transitions [81]: first, we are interested in how boundary conditions would affect particles' dynamics and structure; second, we are curious about how shape could make jamming different; third, we are interested in how thermal fluctuations would play a role near transition points when change system's scale. By investigating these three questions could help us further understand the jamming phase diagram.

In chapter 2, we focused on the role boundary conditions would play upon system's structure and dynamics characteristics near jamming. We observed that smooth boundary induces layer-like structure near the bottom surface. In the mean time, particles' motions along the direction perpendicular to the wall were severely suppressed. Interestingly, when introduced rough boundary condition, a rough wall is like no wall in dense colloidal systems. We further discovered the gradient in dynamics is directly related to gradient in structure. This work provides an alternate way for computer simulations to implement boundary conditions. Besides implications in simulations, in future work, more types of boundary conditions can be tested to determine how

boundary thickness and layer-like structures will change.

In chapter 3, we explored how shape could make a difference when system is jammed by studying non-spherical rods packing and focusing on its structural characteristics. We found gravity acts as a key factor in terms of rods' orientation: instead of randomly distributed, most rods are aligned horizontally. We also revised the model suggested by Desmond and Weeks [30] into a 'three-layer' model: a loosely packed side layer, a more loosely packed top layer, and a more-aligned bottom layer with similar volume fraction ϕ as bulk area. For our next steps, there are two things we are curious to try: first, we can repeat the experiments in 2D and focus on the formation process, since it's much easier to record how rods fall in 2D than 3D. We are interested to determine whether there are preferred structures during the falling process. Second, we can tune the boundary roughness by insert different types of sandpapers. How does boundary layer's thickness change with roughness? Will rods with different aspect ratio behave differently? All those interesting questions are waiting to be explored.

In chapter 4, we focused on critical transitions in the crossover regime of thermal and athermal emulsions. We observed evidence for both glass and jamming transition for our small samples and only observed jamming transition for our large samples, which supports Ikeda's framework [66]. Our rheological data fit well with both HB and TC models and change drastically in shear stress comparing to hydrogel's rheology data [105, 10]. The fitting parameters indicated that there is not a master curves for our samples, nor like hydrogel particles. Given above information, thermal fluctuations do play a important role in liquid-solid transitions. In other words, particles' size matter here. For our future work, tuning particles' size with a broader range could provide more persuasive evidences to support our current results. Besides, observing particles' motion while shearing (using a rheoscope) may provide us direct insights upon local structure/dynamics characteristics near transition points.

In short, we demonstrated that boundary conditions, shape of particles and thermal fluctuation all have nontrivial influences upon jamming behaviors. A more comprehensive jamming diagram is waiting to be completed by conducting similar experiments in other set of systems and numerical simulations.

Bibliography

- [1] D. J. W. Aastuen, N. A. Clark, L. K. Cotter, and Bruce J. Ackerson. Nucleation and growth of colloidal crystals. *Phys. Rev. Lett.*, 57(14):1733–1736, October 1986. doi: 10.1103/physrevlett.57.1733.
- [2] Charles R. A. Abreu, Frederico W. Tavares, and Marcelo Castier. Influence of particle shape on the packing and on the segregation of spherocylinders via monte carlo simulations. *Powder Tech.*, 134(1-2):167–180, August 2003. doi: 10.1016/s0032-5910(03)00151-7.
- [3] Ben R. Aïm and Le P. Goff. Effet de paroi dans les empilements désordonnés de sphères et application à la porosité de mélanges binaires. *Powder Tech.*, 1(5):281–290, 1967.
- [4] Mataz Alcoutlabi and Gregory B. McKenna. Effects of confinement on material behaviour at the nanometre size scale. *J. Phys.: Condens. Matter*, 17(15):R461–R524, April 2005. doi: 10.1088/0953-8984/17/15/r01.
- [5] L. Antl, J. W. Goodwin, R. D. Hill, R. H. Ottewill, S. M. Owens, S. Papworth, and J. A. Waters. The preparation of poly(methyl methacrylate) latices in non-aqueous media. *Colloid Surf.*, 17(1):67–78, January 1986. doi: 10.1016/0166-6622(86)80187-1.
- [6] Roman R. Baglay and Connie B. Roth. Communication: Experimentally determined profile of local glass transition temperature across a glassy-rubbery

- polymer interface with a T_g difference of 80 K. *J. Chem. Phys.*, 143(11):111101, September 2015. doi: 10.1063/1.4931403.
- [7] Roman R. Baglay and Connie B. Roth. Local glass transition temperature $T_g(z)$ of polystyrene next to different polymers: Hard vs. soft confinement. *J. Chem. Phys.*, 146(20):203307, May 2017. doi: 10.1063/1.4975168.
- [8] R. Bandyopadhyay, D. Liang, H. Yardimci, D. A. Sessoms, M. A. Borthwick, S. G. J. Mochrie, J. L. Harden, and R. L. Leheny. Evolution of particle-scale dynamics in an aging clay suspension. *Phys. Rev. Lett.*, 93(22):228302, November 2004. doi: 10.1103/physrevlett.93.228302.
- [9] J. Baschnagel and F. Varnik. Computer simulations of supercooled polymer melts in the bulk and in confined geometry. *J. Phys.: Condens. Matter*, 17(32):R851–R953, July 2005. doi: 10.1088/0953-8984/17/32/r02.
- [10] Anindita Basu, Ye Xu, Tim Still, P. E. Arratia, Zexin Zhang, K. N. Nordstrom, Jennifer M. Rieser, J. P. Gollub, D. J. Durian, and A. G. Yodh. Rheology of soft colloids across the onset of rigidity: scaling behavior, thermal, and non-thermal responses. *Soft Matter*, 10(17):3027–3035, 2014. doi: 10.1039/c3sm52454j.
- [11] Alexandra V. Bayles, Todd M. Squires, and Matthew E. Helgeson. Dark-field differential dynamic microscopy. *Soft Matter*, 12:2440–2452, 2016. doi: 10.1039/C5SM02576A. URL <http://dx.doi.org/10.1039/C5SM02576A>.
- [12] F. Benyahia. On the global and local structural properties of packed beds of nonequilateral cylindrical particles. *Particulate Science and Technology*, 14(3):221–237, July 1996. doi: 10.1080/02726359608906697.
- [13] J. D. Bernal. The Bakerian lecture, 1962. The structure of liquids. *Proc. Roy. Soc. London. Series A*, 280(1382):299–322, July 1964.

- [14] J. Bibette, D. Roux, and B. Pouligny. Creaming of emulsions: the role of depletion forces induced by surfactant. *Journal de Physique II*, 2(3):401–424, March 1992. doi: 10.1051/jp2:1992141.
- [15] Kurt Binder, Jörg Baschnagel, and Wolfgang Paul. Glass transition of polymer melts: Test of theoretical concepts by computer simulation. *Prog. Poly. Sci.*, 28(1):115–172, January 2003. doi: 10.1016/s0079-6700(02)00030-8.
- [16] G. Biroli, J. P. Bouchaud, A. Cavagna, T. S. Grigera, and P. Verrocchio. Thermodynamic signature of growing amorphous order in glass-forming liquids. *Nat. Phys.*, 4(10):771–775, October 2008. doi: 10.1038/nphys1050.
- [17] Daniel Bonn, Morton M. Denn, Ludovic Berthier, Thibaut Divoux, and Sébastien Manneville. Yield stress materials in soft condensed matter. *Rev. Mod. Phys.*, 89:035005, Aug 2017. doi: 10.1103/RevModPhys.89.035005. URL <https://link.aps.org/doi/10.1103/RevModPhys.89.035005>.
- [18] Nicolas Brodu, Joshua A. Dijksman, and Robert P. Behringer. Spanning the scales of granular materials through microscopic force imaging. *Nature Communications*, 6(1):6361, March 2015. ISSN 2041-1723. doi: 10.1038/ncomms7361. URL <https://www.nature.com/articles/ncomms7361>.
- [19] R. L. Brown and P. G. W. Hawksley. Effect of container walls on packing density of particles. *Nature*, 157:585, 1946. doi: 10.1038/157585a0.
- [20] Marco Caggioni, Veronique Trappe, and Patrick T. Spicer. Variations of the herschelbulkley exponent reflecting contributions of the viscous continuous phase to the shear rate-dependent stress of soft glassy materials. *Journal of Rheology*, 64(2):413–422, 2020. doi: 10.1122/1.5120633. URL <https://doi.org/10.1122/1.5120633>.

- [21] P. C. Carman. Fluid flow through granular beds. *Trans. Inst. Chem. Eng.*, 15: 150–166, 1937.
- [22] Dandan Chen, Denis Semwogerere, Jun Sato, Victor Breedveld, and Eric R. Weeks. Microscopic structural relaxation in a sheared supercooled colloidal liquid. *Phys. Rev. E*, 81(1):011403, January 2010. doi: 10.1103/physreve.81.011403.
- [23] Dane Christie, Chuan Zhang, Jie Fu, Bruce Koel, and Rodney D. Priestley. Glass transition temperature of colloidal polystyrene dispersed in various liquids. *J. Poly. Sci. B*, 54(17):1776–1783, September 2016. doi: 10.1002/polb.24082.
- [24] L. Cipelletti and L. Ramos. Slow dynamics in glasses, gels and foams. *Curr. Op. Coll. Int. Sci.*, 7(3-4):228–234, August 2002. doi: 10.1016/s1359-0294(02)00051-1.
- [25] D. Coelho, J. F. Thovert, and P. M. Adler. Geometrical and transport properties of random packings of spheres and aspherical particles. *Phys. Rev. E*, 55(2): 1959–1978, February 1997. doi: 10.1103/physreve.55.1959.
- [26] Rachel E. Courtland and Eric R. Weeks. Direct visualization of ageing in colloidal glasses. *J. Phys.: Condens. Matter*, 15(1):S359–S365, January 2003. doi: 10.1088/0953-8984/15/1/349.
- [27] John C. Crocker and David G. Grier. Methods of digital video microscopy for colloidal studies. *J. Colloid Interface Sci.*, 179(1):298–310, April 1996. doi: 10.1006/jcis.1996.0217.
- [28] T. Davris and A. V. Lyulin. A coarse-grained molecular dynamics study of segmental structure and mobility in capped crosslinked copolymer films. *J. Chem. Phys.*, 143(7):074906, August 2015. doi: 10.1063/1.4928961.

- [29] K. Desmond and Scott V. Franklin. Jamming of three-dimensional prolate granular materials. *Phys. Rev. E*, 73(3):031306, March 2006. doi: 10.1103/physreve.73.031306.
- [30] Kenneth W. Desmond and Eric R. Weeks. Random close packing of disks and spheres in confined geometries. *Phys. Rev. E*, 80(5):051305, November 2009. doi: 10.1103/physreve.80.051305.
- [31] Kenneth W. Desmond and Eric R. Weeks. Influence of particle size distribution on random close packing of spheres. *Phys. Rev. E*, 90(2):022204, August 2014. doi: 10.1103/physreve.90.022204.
- [32] Xiaojun Di, K. Z. Win, Gregory B. McKenna, Tetsuharu Narita, François Lequeux, Srinivasa R. Pullela, and Zhengdong Cheng. Signatures of structural recovery in colloidal glasses. *Phys. Rev. Lett.*, 106(9):095701, February 2011. doi: 10.1103/physrevlett.106.095701.
- [33] M. Dinkgreve, J. Paredes, M. A. J. Michels, and D. Bonn. Universal rescaling of flow curves for yield-stress fluids close to jamming. *Phys. Rev. E*, 92:012305, Jul 2015. doi: 10.1103/PhysRevE.92.012305. URL <https://link.aps.org/doi/10.1103/PhysRevE.92.012305>.
- [34] M. Dinkgreve, M. A. J. Michels, T. G. Mason, and D. Bonn. Crossover between athermal jamming and the thermal glass transition of suspensions. *Phys. Rev. Lett.*, 121:228001, Nov 2018. doi: 10.1103/PhysRevLett.121.228001. URL <https://link.aps.org/doi/10.1103/PhysRevLett.121.228001>.
- [35] A. D. Dinsmore, Eric R. Weeks, Vikram Prasad, Andrew C. Levitt, and D. A. Weitz. Three-dimensional confocal microscopy of colloids. *App. Optics*, 40(24):4152–4159, 2001. doi: 10.1364/AO.40.004152.

- [36] M. D. Ediger and J. A. Forrest. Dynamics near free surfaces and the glass transition in thin polymer films: A view to the future. *Macromolecules*, 47(2): 471–478, January 2014. doi: 10.1021/ma4017696.
- [37] Kazem V. Edmond, Carolyn R. Nugent, and Eric R. Weeks. Influence of confinement on dynamical heterogeneities in dense colloidal samples. *Phys. Rev. E*, 85:041401, April 2012. doi: 10.1103/physreve.85.041401.
- [38] D. El Masri, M. Pierno, L. Berthier, and L. Cipelletti. Ageing and ultra-slow equilibration in concentrated colloidal hard spheres. *J. Phys.: Condens. Matter*, 17(45):S3543–S3549, November 2005. doi: 10.1088/0953-8984/17/45/046.
- [39] Christopher M. Evans, Suresh Narayanan, Zhang Jiang, and John M. Torkelson. Modulus, confinement, and temperature effects on surface capillary wave dynamics in bilayer polymer films near the glass transition. *Phys. Rev. Lett.*, 109:038302, July 2012. doi: 10.1103/physrevlett.109.038302.
- [40] K. E. Evans and M. D. Ferrar. The packing of thick fibres. *J. Phys. D*, 22(2): 354–360, February 1989. doi: 10.1088/0022-3727/22/2/020.
- [41] K. E. Evans and A. G. Gibson. Prediction of the maximum packing fraction achievable in randomly oriented short-fibre composites. *Composites Science and Technology*, 25(2):149–162, January 1986. doi: 10.1016/0266-3538(86)90040-0.
- [42] T. Fehr and H. Löwen. Glass transition in confined geometry. *Phys. Rev. E*, 52(4):4016–4025, October 1995. doi: 10.1103/physreve.52.4016.
- [43] Claudia Ferreiro-Córdova and Jeroen S. van Duijneveldt. Random packing of hard spherocylinders. *J. Chem. Eng. Data*, 59(10):3055–3060, October 2014. doi: 10.1021/je500119r.

- [44] J. Forrest and K. Dalnoki-Veress. The glass transition in thin polymer films. *Adv. Coll. Int. Sci.*, 94(1-3):167–195, November 2001. doi: 10.1016/S0001-8686(01)00060-4.
- [45] E. A. Foumeny and S. Roshani. Mean voidage of packed beds of cylindrical particles. *Chem. Eng. Sci.*, 46(9):2363–2364, 1991. doi: 10.1016/0009-2509(91)85135-k.
- [46] Julian O. Freeman, Sean Peterson, Cong Cao, Yujie Wang, Scott V. Franklin, and Eric R. Weeks. Random packing of rods in small containers. *Granular Matter*, 21(4):84, August 2019. ISSN 1434-7636. doi: 10.1007/s10035-019-0939-x. URL <https://doi.org/10.1007/s10035-019-0939-x>.
- [47] David S. Fryer, Richard D. Peters, Eui J. Kim, Jeanne E. Tomaszewski, Juan J. de Pablo, Paul F. Nealey, Chris C. White, and Wen-li Wu. Dependence of the glass transition temperature of polymer films on interfacial energy and thickness. *Macromolecules*, 34(16):5627–5634, July 2001. doi: 10.1021/ma001932q.
- [48] Yang Fu, Yan Xi, Yixin Cao, and Yujie Wang. X-ray microtomography study of the compaction process of rods under tapping. *Phys. Rev. E*, 85(5), May 2012.
- [49] Mingle Gan, Nishanth Gopinathan, Xiaodong Jia, and Richard A. Williams. Predicting packing characteristics of particles of arbitrary shapes. *KONA Powder and Particle Journal*, 22(0):82–93, 2004. doi: 10.14356/kona.2004012.
- [50] K. S. Gautam, A. D. Schwab, A. Dhinojwala, D. Zhang, S. M. Dougal, and M. S. Yeganeh. Molecular structure of polystyrene at air/polymer and solid/polymer interfaces. *Phys. Rev. Lett.*, 85(18):3854–3857, October 2000. doi: 10.1103/physrevlett.85.3854.

- [51] Peter Gin, Naisheng Jiang, Chen Liang, Takashi Taniguchi, Bulent Akgun, Sushil K. Satija, Maya K. Endoh, and Tadanori Koga. Revealed architectures of adsorbed polymer chains at solid-polymer melt interfaces. *Phys. Rev. Lett.*, 109(26):265501, December 2012. doi: 10.1103/physrevlett.109.265501.
- [52] Thomas C. Hales. A proof of the Kepler conjecture. *Ann. Math.*, 162:1065–1185, 2005. doi: 10.4007/annals.2005.162.1065.
- [53] Thomas C. Hales, John Harrison, Sean McLaughlin, Tobias Nipkow, Steven Obua, and Roland Zumkeller. A revision of the proof of the Kepler conjecture. *Discrete and Computational Geometry*, 44:1–34, 2010. doi: 10.1007/s00454-009-9148-4.
- [54] Paul Z. Hanakata, Jack F. Douglas, and Francis W. Starr. Local variation of fragility and glass transition temperature of ultra-thin supported polymer films. *J. Chem. Phys.*, 137(24):244901, December 2012. doi: 10.1063/1.4772402.
- [55] Paul Z. Hanakata, Jack F. Douglas, and Francis W. Starr. Interfacial mobility scale determines the scale of collective motion and relaxation rate in polymer films. *Nature Comm.*, 5:4163, June 2014. doi: 10.1038/ncomms5163.
- [56] Paul Z. Hanakata, Beatriz A. Pazmiño Betancourt, Jack F. Douglas, and Francis W. Starr. A unifying framework to quantify the effects of substrate interactions, stiffness, and roughness on the dynamics of thin supported polymer films. *J. Chem. Phys.*, 142(23):234907, June 2015. doi: 10.1063/1.4922481.
- [57] F. He, L. M. Wang, and R. Richert. Confined viscous liquids: Interfacial versus finite size effects. *Euro. Phys. J. - Special Topics*, 141(1):3–9, February 2007. doi: 10.1140/epjst/e2007-00008-0.
- [58] P. Anne Hiltner and Irvin M. Krieger. Diffraction of light by ordered

- suspensions, May 2002. URL <https://pubs.acs.org/doi/pdf/10.1021/j100727a049>.
- [59] K. Hima Nagamanasa, Shreyas Gokhale, A. K. Sood, and Rajesh Ganapathy. Direct measurements of growing amorphous order and non-monotonic dynamic correlations in a colloidal glass-former. *Nature Phys.*, 11(5):403–408, April 2015. doi: 10.1038/nphys3289.
- [60] Glen M. Hocky, Ludovic Berthier, Walter Kob, and David R. Reichman. Crossovers in the dynamics of supercooled liquids probed by an amorphous wall. *Phys. Rev. E*, 89(5):052311, May 2014. doi: 10.1103/physreve.89.052311.
- [61] Xinru Huang and Connie B. Roth. Changes in the temperature-dependent specific volume of supported polystyrene films with film thickness. *J. Chem. Phys.*, 144(23):234903, June 2016. doi: 10.1063/1.4953855.
- [62] Y. Huang and D. R. Paul. Physical aging of thin glassy polymer films monitored by gas permeability. *Polymer*, 45(25):8377–8393, November 2004. doi: 10.1016/j.polymer.2004.10.019.
- [63] Dmytro Hudzinsky, Alexey V. Lyulin, Arlette R. C. Baljon, Nikolay K. Balabaev, and Matthias A. J. Michels. Effects of strong confinement on the glass-transition temperature in simulated atactic polystyrene films. *Macromolecules*, 44(7):2299–2310, March 2011. doi: 10.1021/ma102567s.
- [64] Gary L. Hunter and Eric R. Weeks. The physics of the colloidal glass transition. *Rep. Prog. Phys.*, 75(6):066501, May 2012. doi: 10.1088/0034-4885/75/6/066501.
- [65] Gary L. Hunter, Kazem V. Edmond, and Eric R. Weeks. Boundary mobility controls glassiness in confined colloidal liquids. *Phys. Rev. Lett.*, 112(21):218302, May 2014. doi: 10.1103/physrevlett.112.218302.

- [66] Atsushi Ikeda, Ludovic Berthier, and Peter Sollich. Unified study of glass and jamming rheology in soft particle systems. *Phys. Rev. Lett.*, 109:018301, July 2012. doi: 10.1103/physrevlett.109.018301.
- [67] H. M. Jaeger and Sidney R. Nagel. Physics of the granular state. *Science*, 255(5051):1523–1531, March 1992. doi: 10.1126/science.255.5051.1523.
- [68] X. Jia, M. Gan, R. A. Williams, and D. Rhodes. Validation of a digital packing algorithm in predicting powder packing densities. *Powder Tech.*, 174(1-2):10–13, May 2007. doi: 10.1016/j.powtec.2006.10.013.
- [69] Richard A. L. Jones. *Soft Condensed Matter (Oxford Master Series in Condensed Matter Physics, Vol. 6)*. Oxford University Press, 1st edition, August 2002. ISBN 0198505892.
- [70] Gergely Keledi, Jozsef Hari, and Bela Pukanszky. Polymer nanocomposites: structure, interaction, and functionality. *Nanoscale*, 4(6):1919–1938, 2012. doi: 10.1039/c2nr11442a.
- [71] Roland Kjellander and Sten Sarman. Pair correlations of non-uniform hard-sphere fluids in narrow slits and the mechanism of oscillatory solvation forces. *J. Chem. Soc. Faraday Trans.*, 87(12):1869–1881, 1991. doi: 10.1039/ft9918701869.
- [72] James B. Knight, Christopher G. Fandrich, Chun N. Lau, Heinrich M. Jaeger, and Sidney R. Nagel. Density relaxation in a vibrated granular material. *Phys. Rev. E*, 51(5):3957–3963, May 1995. doi: 10.1103/physreve.51.3957.
- [73] W. Kob, P. Scheidler, and K. Binder. The relaxation dynamics of a simple glass former confined in a pore. *Europhys. Lett.*, 52(3):277–283, 2000.

- [74] Vladimir Kobelev and Kenneth S. Schweizer. Strain softening, yielding, and shear thinning in glassy colloidal suspensions. *Phys. Rev. E*, 71:021401, Feb 2005. doi: 10.1103/PhysRevE.71.021401. URL <https://link.aps.org/doi/10.1103/PhysRevE.71.021401>.
- [75] J. M. Kosterlitz and D. J. Thouless. Ordering, metastability and phase transitions in two-dimensional systems. *J. Phys. C: Solid State Physics*, 6(7):1181–1203, April 1973. doi: 10.1088/0022-3719/6/7/010.
- [76] Daniela J. Kraft, Jan Hilhorst, Maria A. P. Heinen, Mathijs J. Hoogenraad, Bob Luigjes, and Willem K. Kegel. Patchy Polymer Colloids with Tunable Anisotropy Dimensions. *The Journal of Physical Chemistry B*, 115(22):7175–7181, June 2011. ISSN 1520-6106, 1520-5207. doi: 10.1021/jp108760g. URL <https://pubs.acs.org/doi/10.1021/jp108760g>.
- [77] James W. Landry, Gary S. Grest, Leonardo E. Silbert, and Steven J. Plimpton. Confined granular packings: Structure, stress, and forces. *Phys. Rev. E*, 67(4):041303, April 2003. doi: 10.1103/PhysRevE.67.041303.
- [78] Ryan J. Lang and David S. Simmons. Interfacial dynamic length scales in the glass transition of a model freestanding polymer film and their connection to cooperative motion. *Macromolecules*, 46(24):9818–9825, December 2013. doi: 10.1021/ma401525q.
- [79] Yan-Wei Li, Wen-Sheng Xu, and Zhao-Yan Sun. Growing point-to-set length scales in Lennard-Jones glass-forming liquids. *J. Chem. Phys.*, 140(12):124502, March 2014. doi: 10.1063/1.4868987.
- [80] H. M. Lindsay and P. M. Chaikin. Elastic properties of colloidal crystals and glasses. *J. Chem. Phys.*, 76(7):3774–3781, 1982. doi: 10.1063/1.443417.

- [81] Andrea J. Liu and Sidney R. Nagel. Jamming is not just cool any more. *Nature*, 396(6706):21–22, November 1998. doi: 10.1038/23819.
- [82] Andrea J. Liu and Sidney R. Nagel. The jamming transition and the marginally jammed solid. *Ann. Rev. Cond. Mat. Phys.*, 1(1):347–369, 2010. doi: 10.1146/annurev-conmatphys-070909-104045.
- [83] Yanyan Liu, Kazem V. Edmond, Arran Curran, Charles Bryant, Bo Peng, Dirk G. A. L. Aarts, Stefano Sacanna, and Roel P. A. Dullens. Coreshell particles for simultaneous 3d imaging and optical tweezing in dense colloidal materials. *Advanced Materials*, 28(36):8001–8006, 2016. doi: 10.1002/adma.201602137. URL <https://onlinelibrary.wiley.com/doi/abs/10.1002/adma.201602137>.
- [84] G. Lumay and N. Vandewalle. Compaction of anisotropic granular materials: Experiments and simulations. *Phys. Rev. E*, 70(5):051314, November 2004. doi: 10.1103/physreve.70.051314.
- [85] Jennifer M. Lynch, Gianguido C. Cianci, and Eric R. Weeks. Dynamics and structure of an aging binary colloidal glass. *Phys. Rev. E*, 78(3):031410, September 2008. doi: 10.1103/physreve.78.031410.
- [86] M. C. Marchetti, J. F. Joanny, S. Ramaswamy, T. B. Liverpool, J. Prost, Madan Rao, and R. Aditi Simha. Hydrodynamics of soft active matter. *Rev. Mod. Phys.*, 85:1143–1189, Jul 2013. doi: 10.1103/RevModPhys.85.1143. URL <https://link.aps.org/doi/10.1103/RevModPhys.85.1143>.
- [87] Louise Marshall and Charles F. Zukoski. Experimental studies on the rheology of hard-sphere suspensions near the glass transition. *J. Phys. Chem.*, 94(3): 1164–1171, February 1990. doi: 10.1021/j100366a030.
- [88] V. A. Martinez, G. Bryant, and W. van Meegen. Slow dynamics and aging of a

- colloidal hard sphere glass. *Phys. Rev. Lett.*, 101(13):135702, September 2008. doi: 10.1103/physrevlett.101.135702.
- [89] V. A. Martinez, G. Bryant, and W. van Meegen. Aging dynamics of colloidal hard sphere glasses. *J. Chem. Phys.*, 133(11):114906, September 2010. doi: 10.1063/1.3478542.
- [90] T. G. Mason, J. Bibette, and D. A. Weitz. Elasticity of compressed emulsions. *Phys. Rev. Lett.*, 75(10):2051–2054, September 1995. doi: 10.1103/physrevlett.75.2051.
- [91] T. G. Mason, J. Bibette, and D. A. Weitz. Yielding and flow of monodisperse emulsions. *J. Colloid Interface Sci.*, 179(2):439–448, May 1996. doi: 10.1006/jcis.1996.0235.
- [92] T G Mason, J N Wilking, K Meleson, C B Chang, and S M Graves. Nanoemulsions: formation, structure, and physical properties. *Journal of Physics: Condensed Matter*, 18(41):R635–R666, sep 2006. doi: 10.1088/0953-8984/18/41/r01. URL <https://doi.org/10.1088/0953-8984/18/41/r01>.
- [93] Gregory B. McKenna. Mechanical rejuvenation in polymer glasses: fact or fallacy? *J. Phys.: Condens. Matter*, 15(11):S737–S763, March 2003. doi: 10.1088/0953-8984/15/11/301.
- [94] Gregory B. McKenna, Tetsuharu Narita, and François Lequeux. Soft colloidal matter: A phenomenological comparison of the aging and mechanical responses with those of molecular glasses. *J. Rheo.*, 53(3):489–516, May 2009. doi: 10.1122/1.3092933.
- [95] Jan Mewis and Norman J Wagner. *Colloidal suspension rheology*. Cambridge University Press, 2012.

- [96] J. V. Milewski. The combined packing of rods and spheres in reinforcing plastics. *Ind. Eng. Chem. Prod. Res. Dev.*, 17(4):363–366, December 1978. doi: 10.1021/i360068a016.
- [97] Jeetain Mittal, Thomas M. Truskett, Jeffrey R. Errington, and Gerhard Hummer. Layering and position-dependent diffusive dynamics of confined fluids. *Phys. Rev. Lett.*, 100(14):145901, April 2008. doi: 10.1103/physrevlett.100.145901.
- [98] A. Montillet and L. Le Coq. Characteristics of fixed beds packed with anisotropic particles Use of image analysis. *Powder Tech.*, 121(2-3):138–148, November 2001. doi: 10.1016/s0032-5910(01)00332-1.
- [99] Sidney R. Nagel. Experimental soft-matter science. *Rev. Mod. Phys.*, 89:025002, Apr 2017. doi: 10.1103/RevModPhys.89.025002. URL <https://link.aps.org/doi/10.1103/RevModPhys.89.025002>.
- [100] Simone Napolitano, Simona Capponi, and Bram Vanroy. Glassy dynamics of soft matter under 1D confinement: How irreversible adsorption affects molecular packing, mobility gradients and orientational polarization in thin films. *Euro. Phys. J. E*, 36(6):1–37, 2013. doi: 10.1140/epje/2013-13061-8.
- [101] Simone Napolitano, Emmanouil Glynos, and Nicholas B. Tito. Glass transition of polymers in bulk, confined geometries, and near interfaces. *Rep. Prog. Phys.*, 80(3):036602, March 2017. doi: 10.1088/1361-6633/aa5284.
- [102] M. Nardin, E. Papirer, and J. Schultz. Contribution à l'étude des empilements au hasard de fibres et/ou de particules sphériques. *Powder Tech.*, 44(2):131–140, November 1985. doi: 10.1016/0032-5910(85)87019-4.
- [103] Takayuki Narumi, Scott V. Franklin, Kenneth W. Desmond, Michio Tokuyama, and Eric R. Weeks. Spatial and temporal dynamical heterogeneities approaching

- the binary colloidal glass transition. *Soft Matter*, 7(4):1472–1482, 2011. doi: 10.1039/c0sm00756k.
- [104] Z. T. Németh and H. Löwen. Freezing and glass transition of hard spheres in cavities. *Phys. Rev. E*, 59(6):6824–6829, June 1999. doi: 10.1103/physreve.59.6824.
- [105] K. N. Nordstrom, E. Verneuil, P. E. Arratia, A. Basu, Z. Zhang, A. G. Yodh, J. P. Gollub, and D. J. Durian. Microfluidic rheology of soft colloids above and below jamming. *Phys. Rev. Lett.*, 105(17):175701, September 2010. doi: 10.1103/physrevlett.105.175701.
- [106] M. Novellani, R. Santini, and L. Tadrist. Experimental study of the porosity of loose stacks of stiff cylindrical fibres: Influence of the aspect ratio of fibres. *European Physical Journal B*, 13(3):571–578, 2000. doi: 10.1007/s100510050069.
- [107] Corey S. O’Hern, Leonardo E. Silbert, Andrea J. Liu, and Sidney R. Nagel. Jamming at zero temperature and zero applied stress: The epitome of disorder. *Phys. Rev. E*, 68:011306, Jul 2003. doi: 10.1103/PhysRevE.68.011306. URL <https://link.aps.org/doi/10.1103/PhysRevE.68.011306>.
- [108] Peter Olsson and S. Teitel. Critical scaling of shear viscosity at the jamming transition. *Phys. Rev. Lett.*, 99(17):178001, October 2007. doi: 10.1103/physrevlett.99.178001.
- [109] Peter Olsson and S. Teitel. Critical scaling of shearing rheology at the jamming transition of soft-core frictionless disks. *Phys. Rev. E*, 83(3):030302, March 2011. doi: 10.1103/physreve.83.030302.
- [110] Keewook Paeng, Ranko Richert, and M. D. Ediger. Molecular mobility in supported thin films of polystyrene, poly(methyl methacrylate), and poly(2-

- vinyl pyridine) probed by dye reorientation. *Soft Matter*, 8(3):819–826, 2012. doi: 10.1039/c1sm06501g.
- [111] José Paredes, Matthias A. J. Michels, and Daniel Bonn. Rheology across the zero-temperature jamming transition. *Phys. Rev. Lett.*, 111:015701, Jul 2013. doi: 10.1103/PhysRevLett.111.015701. URL <https://link.aps.org/doi/10.1103/PhysRevLett.111.015701>.
- [112] J. G. Parkhouse and A. Kelly. The random packing of fibres in three dimensions. *Proc. Roy. Soc. London A*, 451(1943):737–746, December 1995. doi: 10.1098/rspa.1995.0152.
- [113] G Petekidis, D Vlassopoulos, and P N Pusey. Yielding and flow of sheared colloidal glasses. *Journal of Physics: Condensed Matter*, 16(38):S3955–S3963, sep 2004. doi: 10.1088/0953-8984/16/38/013. URL <https://doi.org/10.1088/0953-8984/16/38/013>.
- [114] Simone Peter, Hendrik Meyer, and Jörg Baschnagel. Thickness-dependent reduction of the glass-transition temperature in thin polymer films with a free surface. *J. Poly. Sci. B: Polymer Physics*, 44(20):2951–2967, October 2006. doi: 10.1002/polb.20924.
- [115] Albert P. Philipse. The random contact equation and its implications for (colloidal) rods in packings, suspensions, and anisotropic powders. *Langmuir*, 12(5):1127–1133, January 1996. doi: 10.1021/la950671o.
- [116] Wilson C. K. Poon, Eric R. Weeks, and C. Patrick Royall. On measuring colloidal volume fractions. *Soft Matter*, 8(1):21–30, 2012. doi: 10.1039/c1sm06083j.
- [117] Rodney D. Priestley. Physical aging of confined glasses. *Soft Matter*, 5(5):919–926, 2009. doi: 10.1039/b816482g.

- [118] Rodney D. Priestley, Christopher J. Ellison, Linda J. Broadbelt, and John M. Torkelson. Structural relaxation of polymer glasses at surfaces, interfaces, and in between. *Science*, 309(5733):456–459, July 2005. doi: 10.1126/science.1112217.
- [119] P. N. Pusey and W. van Megen. Phase behaviour of concentrated suspensions of nearly hard colloidal spheres. *Nature*, 320(6060):340–342, March 1986. doi: 10.1038/320340a0.
- [120] Justin E. Pye, Kate A. Rohald, Elizabeth A. Baker, and Connie B. Roth. Physical aging in ultrathin polystyrene films: Evidence of a gradient in dynamics at the free surface and its connection to the glass transition temperature reductions. *Macromolecules*, 43(19):8296–8303, September 2010. doi: 10.1021/ma101412r.
- [121] Ouamar Rahli, Lounès Tadrist, and Robert Blanc. Experimental analysis of the porosity of randomly packed rigid fibers. *Comptes Rendus de l'Académie des Sciences - Series IIB*, 327(8):725–729, August 1999. doi: 10.1016/s1287-4620(99)80127-6.
- [122] Pedro Ramírez-González and Magdaleno Medina-Noyola. Aging of a homogeneously quenched colloidal glass-forming liquid. *Phys. Rev. E*, 82(6):061504, December 2010. doi: 10.1103/physreve.82.061504.
- [123] Patrick Richard, Mario Nicodemi, Renaud Delannay, Philippe Ribiere, and Daniel Bideau. Slow relaxation and compaction of granular systems. *Nat. Mater.*, 4(2):121–128, February 2005. doi: 10.1038/nmat1300.
- [124] R. Richert. Dynamics of nanoconfined supercooled liquids. *Ann. Rev. Phys. Chem.*, 62(1):65–84, 2011. doi: 10.1146/annurev-physchem-032210-103343.
- [125] L. H. S. Roblee, R. M. Baird, and J. W. Tierney. Radial porosity variations in

- packed beds. *AIChE Journal*, 4(4):460–464, December 1958. doi: 10.1002/aic.690040415.
- [126] R. O. Rosenberg, D. Thirumalai, and R. D. Mountain. Liquid, crystalline and glassy states of binary charged colloidal suspensions. *J. Phys.: Condens. Matter*, 1(11):2109–2114, March 1989. doi: 10.1088/0953-8984/1/11/019.
- [127] C. B. Roth, K. L. McNerny, W. F. Jager, and J. M. Torkelson. Eliminating the enhanced mobility at the free surface of polystyrene: fluorescence studies of the glass transition temperature in thin bilayer films of immiscible polymers. *Macromolecules*, 40(7):2568–2574, April 2007. doi: 10.1021/ma062864w.
- [128] Connie B. Roth and John R. Dutcher. Glass transition and chain mobility in thin polymer films. *J. Electroanalytical Chem.*, 584(1):13–22, October 2005. doi: 10.1016/j.jelechem.2004.03.003.
- [129] S. Sacanna, L. Rossi, A. Wouterse, and A. P. Philipse. Observation of a shape-dependent density maximum in random packings and glasses of colloidal silica ellipsoids. *J. Phys.: Condens. Matter*, 19(37):376108, September 2007. doi: 10.1088/0953-8984/19/37/376108.
- [130] Mohammad S. Safari, Maria A. Vorontsova, Ryan Poling-Skutvik, Peter G. Vekilov, and Jacinta C. Conrad. Differential dynamic microscopy of weakly scattering and polydisperse protein-rich clusters. *Phys. Rev. E*, 92:042712, Oct 2015. doi: 10.1103/PhysRevE.92.042712. URL <https://link.aps.org/doi/10.1103/PhysRevE.92.042712>.
- [131] Philip Geoffrey Saffman and Geoffrey Ingram Taylor. The penetration of a fluid into a porous medium or Hele-Shaw cell containing a more viscous liquid. *Proceedings of the Royal Society of London. Series A. Mathematical and Physical*

- Sciences*, 245(1242):312–329, June 1958. doi: 10.1098/rspa.1958.0085. URL <https://royalsocietypublishing.org/doi/10.1098/rspa.1958.0085>.
- [132] Prasad S. Sarangapani, Andrew B. Schofield, and Yingxi Zhu. Direct experimental evidence of growing dynamic length scales in confined colloidal liquids. *Phys. Rev. E*, 83(3):030502, March 2011. doi: 10.1103/physreve.83.030502.
- [133] Prasad S. Sarangapani, Andrew B. Schofield, and Yingxi Zhu. Relationship between cooperative motion and the confinement length scale in confined colloidal liquids. *Soft Matter*, 8(3):814–818, 2012. doi: 10.1039/c1sm06502e.
- [134] Frank Scheffold, Frédéric Cardinaux, and Thomas G Mason. Linear and non-linear rheology of dense emulsions across the glass and the jamming regimes. *Journal of Physics: Condensed Matter*, 25(50):502101, 2013.
- [135] P. Scheidler, W. Kob, and K. Binder. Cooperative motion and growing length scales in supercooled confined liquids. *Europhys. Lett.*, 59(5):701–707, 2002. doi: 10.1209/epl/i2002-00182-9.
- [136] P. Scheidler, W. Kob, and K. Binder. The relaxation dynamics of a supercooled liquid confined by rough walls. *J. Phys. Chem. B*, 108(21):6673–6686, March 2004. doi: 10.1021/jp036593s.
- [137] David G. Scott. Packing of spheres: Packing of equal spheres. *Nature*, 188(4754):908–909, December 1960. doi: 10.1038/188908a0.
- [138] G. T. Seidler, G. Martinez, L. H. Seeley, K. H. Kim, E. A. Behne, S. Zaranek, B. D. Chapman, S. M. Heald, and D. L. Brewe. Granule-by-granule reconstruction of a sandpile from x-ray microtomography data. *Phys. Rev. E*, 62(6):8175–8181, December 2000. doi: 10.1103/physreve.62.8175.

- [139] Mani Sen, Naisheng Jiang, Justin Cheung, Maya K. Endoh, Tadanori Koga, Daisuke Kawaguchi, and Keiji Tanaka. Flattening process of polymer chains irreversibly adsorbed on a solid. *ACS Macro Lett.*, 5(4):504–508, April 2016. doi: 10.1021/acsmacrolett.6b00169.
- [140] Grant D. Smith, Dmitry Bedrov, and Oleg Borodin. Structural relaxation and dynamic heterogeneity in a polymer melt at attractive surfaces. *Phys. Rev. Lett.*, 90(22):226103, June 2003. doi: 10.1103/physrevlett.90.226103.
- [141] K. Stokely, A. Diacou, and Scott V. Franklin. Two-dimensional packing in prolate granular materials. *Phys. Rev. E*, 67:051302, May 2003. doi: 10.1103/physreve.67.051302.
- [142] L. C. E. Struik. Physical aging in plastics and other glassy materials. *Polym. Eng. Sci.*, 17(3):165–173, March 1977. doi: 10.1002/pen.760170305.
- [143] Henna Tangri, Yu Guo, and Jennifer S. Curtis. Packing of cylindrical particles: DEM simulations and experimental measurements. *Powder Tech.*, 317:72–82, July 2017. doi: 10.1016/j.powtec.2017.03.058.
- [144] M. R. Tant and G. L. Wilkes. An overview of the nonequilibrium behavior of polymer glasses. *Polym. Eng. Sci.*, 21(14):874–895, 1981. doi: 10.1002/pen.760211403.
- [145] S. Torquato, T. M. Truskett, and P. G. Debenedetti. Is random close packing of spheres well defined? *Phys. Rev. Lett.*, 84(10):2064–2067, March 2000. doi: 10.1103/physrevlett.84.2064.
- [146] M. Trepanier and Scott V. Franklin. Column collapse of granular rods. *Phys. Rev. E*, 82:011308, July 2010. doi: 10.1103/physreve.82.011308.

- [147] O. K. C. Tsui, T. P. Russell, and C. J. Hawker. Effect of interfacial interactions on the glass transition of polymer thin films. *Macromolecules*, 34(16):5535–5539, July 2001. doi: 10.1021/ma000028v.
- [148] J. Ugelstad, P. C. Mørk, Kaggerud, T. Ellingsen, and A. Berge. Swelling of oligomer-polymer particles. new methods of preparation. *Adv. Coll. Int. Sci.*, 13(1-2):101–140, April 1980. doi: 10.1016/0001-8686(80)87003-5.
- [149] Casper van der Wel, Rohit K. Bhan, Ruben W. Verweij, Hans C. Frijters, Zhe Gong, Andrew D. Hollingsworth, Stefano Sacanna, and Daniela J. Kraft. Preparation of Colloidal Organosilica Spheres through Spontaneous Emulsification. *Langmuir*, 33(33):8174–8180, August 2017. ISSN 0743-7463. doi: 10.1021/acs.langmuir.7b01398. URL <https://doi.org/10.1021/acs.langmuir.7b01398>.
- [150] W. van Meegen, T. C. Mortensen, S. R. Williams, and J. Müller. Measurement of the self-intermediate scattering function of suspensions of hard spherical particles near the glass transition. *Phys. Rev. E*, 58(5):6073–6085, November 1998. doi: 10.1103/physreve.58.6073.
- [151] F. Varnik and K. Binder. Shear viscosity of a supercooled polymer melt via nonequilibrium molecular dynamics simulations. *J. Chem. Phys.*, 117(13):6336–6349, 2002. doi: 10.1063/1.1503770.
- [152] F. Varnik, J. Baschnagel, and K. Binder. Reduction of the glass transition temperature in polymer films: A molecular-dynamics study. *Phys. Rev. E*, 65:021507, January 2002. doi: 10.1103/physreve.65.021507.
- [153] F. Varnik, J. Baschnagel, and K. Binder. Static and dynamic properties of supercooled thin polymer films. *Euro. Phys. J. E*, 8(2):175–192, 2002. doi: 10.1140/epje\%252fi2001-10092-8.

- [154] L. C. Verman and S. Banerjee. Effect of container walls on packing density of particles. *Nature*, 157:584, 1946. doi: 10.1038/157584b0.
- [155] Fernando X. Villarruel, Benjamin E. Lauderdale, Daniel M. Mueth, and Heinrich M. Jaeger. Compaction of rods: Relaxation and ordering in vibrated, anisotropic granular material. *Phys. Rev. E*, 61(6):6914–6921, June 2000. doi: 10.1103/PhysRevE.61.6914. URL <https://link.aps.org/doi/10.1103/PhysRevE.61.6914>.
- [156] Jinhua Wang and Gregory B. McKenna. Viscoelastic and glass transition properties of ultrathin polystyrene films by dewetting from liquid glycerol. *Macromolecules*, 46(6):2485–2495, March 2013. doi: 10.1021/ma400040j.
- [157] Mu Wang and John F. Brady. Constant stress and pressure rheology of colloidal suspensions. *Phys. Rev. Lett.*, 115:158301, Oct 2015. doi: 10.1103/PhysRevLett.115.158301. URL <https://link.aps.org/doi/10.1103/PhysRevLett.115.158301>.
- [158] Eric R. Weeks. Melting colloidal crystals from the inside out. *Science*, 338(6103):55–56, October 2012. doi: 10.1126/science.1228952.
- [159] Eric R. Weeks and D. A. Weitz. Properties of cage rearrangements observed near the colloidal glass transition. *Phys. Rev. Lett.*, 89(9):095704, August 2002. doi: 10.1103/physrevlett.89.095704.
- [160] S. R. Williams and A. P. Philipse. Random packings of spheres and spherocylinders simulated by mechanical contraction. *Phys. Rev. E*, 67(5):051301, May 2003. doi: 10.1103/physreve.67.051301.
- [161] Vikrant Yadav, Jean-Yonnel Chastaing, and Arshad Kudrolli. Effect of aspect ratio on the development of order in vibrated granular rods. *Phys. Rev. E*, 88

- (5):052203, November 2013. doi: 10.1103/PhysRevE.88.052203. URL <https://link.aps.org/doi/10.1103/PhysRevE.88.052203>.
- [162] K. Yaman, M. Jeng, P. Pincus, C. Jeppesen, and C. M. Marques. Rods near curved surfaces and in curved boxes. *Physica A: Statistical Mechanics and its Applications*, 247(1-4):159–182, December 1997. doi: 10.1016/s0378-4371(97)00405-6.
- [163] Peter Yunker, Zexin Zhang, Kevin Aptowicz, and A. Yodh. Irreversible rearrangements, correlated domains, and local structure in aging glasses. *Phys. Rev. Lett.*, 103(11):115701, September 2009. doi: 10.1103/physrevlett.103.115701.
- [164] Wenli Zhang, Karsten E. Thompson, Allen H. Reed, and Liese Beenken. Relationship between packing structure and porosity in fixed beds of equilateral cylindrical particles. *Chem. Eng. Sci.*, 61(24):8060–8074, December 2006. doi: 10.1016/j.ces.2006.09.036.
- [165] Xiao-Dan Zhang, Cheng-Jie Xia, Xiang-Hui Xiao, and Yu-Jie Wang. Fast synchrotron x-ray tomography study of the packing structures of rods with different aspect ratios. *Chinese Physics B*, 23(4):044501, April 2014. doi: 10.1088/1674-1056/23/4/044501.
- [166] Jian Zhao, Shuixiang Li, Ruiping Zou, and Aibing Yu. Dense random packings of spherocylinders. *Soft Matter*, 8(4):1003–1009, 2012. doi: 10.1039/c1sm06487h.
- [167] R. P. Zou and A. B. Yu. Wall effect on the packing of cylindrical particles. *Chem. Eng. Sci.*, 51(7):1177–1180, April 1996. doi: 10.1016/s0009-2509(96)80017-0.